

Applications of Chalcogen bonding

by

Thomas Fellowes

ORCID: 0000-0002-6389-6049

A thesis submitted in total fulfillment for the
degree of Doctor of Philosophy

in the
Faculty of Science
School of Chemistry and Bio21 Institute
THE UNIVERSITY OF MELBOURNE

March 2021

Contents

List of Figures	v
List of Tables	vii
Abbreviations	ix
Constants	xi
Symbols	xiii
I The strength and nature of chalcogen bonding	1
1 Insights from co-crystal structures	3
1.1 Abstract	3
1.2 Introduction	4
1.3 Results and Discussion	5
1.3.1 Synthesis of benzisoselenazolone derivatives 1a and 1b	5
1.4 Co-crystal structures of benzisoselenazolinones and Lewis bases	5
1.4.1 Effects of the benzisoselenazolone on Ch-bond strength	6
1.4.2 Endocyclic bond lengthening associated with stronger complexes	6
1.4.3 H-bond enhanced Ch-bonding	7
1.4.4 Effects of the Lewis base on Ch-bond strength	8
1.4.5 DFT interaction energies, NBO and NEDA analysis	9
1.5 Conclusion	10
1.6 Supplementary materials	11
1.6.1 Synthetic procedures	11
1.6.1.1 Preparation of 1a	11
1.6.1.2 Preparation of 1b	11
1.6.1.3 Preparation of 3	12
1.6.2 Crystallographic data	12
1.6.2.1 Crystal data for 1a ·DMAP	12
1.6.2.2 Crystal data for 1b	13
1.6.2.3 Crystal data for 1b ·DMAP·H ₂ O	13
1.6.2.4 Crystal data for 1b ·DMAP	13
1.6.2.5 Crystal data for 1b ·quinuclidine	13
1.6.2.6 Crystal data for 1b ·DABCO	14
1.6.2.7 Crystal data for 3	14
1.6.2.8 Crystal data for 3 ·pyridine	14

1.6.2.9	Crystal data for 3 ·DMAP	14
2	Further investigations into Ch-bonded complexes	19
2.1	Introduction	19
2.2	Results and discussion	19
2.2.1	Hammett plots of crystallographic data	22
2.2.2	Measurement of chemical shift anisotropy	28
2.2.2.1	Measurement of CSA in a single crystal	35
2.2.3	Solution-phase studies	35
2.2.3.1	NMR titration experiments	36
2.2.3.2	UV-Vis titration experiment	39
2.2.4	Ch-bonding in the gas phase	40
2.3	Supplementary materials	42
2.3.1	Synthetic procedures	42
2.3.1.1	Preparation of 5	42
2.3.1.2	Preparation of 6	43
2.3.1.3	General procedure for the preparation of benzisoselenazolinone derivatives (procedure A)	43
2.3.1.4	Procedure for the preparation of benzisoselenazolinone derivatives (procedure B)	43
Ebselen 1a	43	
4-Nitro ebselen 1d	44	
4-Cyano ebselen 1e	44	
4-Trifluoromethyl ebselen 1f	44	
4-Bromo ebselen 1g	44	
4-Carboxyethyl ebselen 1h	45	
4-Methyl ebselen 1i	45	
4-Methoxy ebselen 1j	45	
4-Ethoxy ebselen 1k	45	
2.3.2	Crystallisation methods	45

List of Figures

1.1	Synthesis of Ch-bond donors 1a , 1b and 3	5
1.2	Structure of 1b ·DMAP, showing the two distinct geometries.	7
1.3	Structure of 1b ·DMAP·H ₂ O.	7
1.4	Pyridine and DMAP adducts of Se-tetracycle 3	8
1.5	Adducts of benziselenazolinone 1b with quinuclidine and DABCO.	9
1.6	Interaction energies for various complexes.	10
1.7	Orbital overlap for 1a ·DMAP.	10
2.1	Hammett plot of endocyclic Se–N bond length of uncomplexed ebselen derivatives.	22
2.2	One dimensional chains formed by Ch-bonding between the selenium and carbonyl oxygen in 1i . All other ebselen derivatives display a similar packing motif.	23
2.3	Hammett plots of endocyclic Se–N bond length and Se···N Ch-bond length of ebselen derivatives complexed with DMAP. The lines are described by the equations $r(\text{Se}-\text{N}) = (1.957(5) + 0.054(12) \times \sigma_X)$ Å and $r(\text{Se}\cdots\text{N}) = (2.385(17) - 0.15(4) \times \sigma_X)$ Å.	23
2.4	Hammett plots of endocyclic Se–N bond length and Se···N Ch-bond length of ebselen derivatives complexed with 4a . The lines are described by the equations $r(\text{Se}-\text{N}) = (1.9788(32) - 0.024(9) \times \sigma_X)$ Å ($R^2 = 0.5722$) and $r(\text{Se}-\text{N}) = (2.331(14) - 0.04(4) \times \sigma_X)$ Å ($R^2 = 0.1588$)	24
2.5	Hammett plots of endocyclic Se–N bond length and Se···N Ch-bond length of ebselen derivatives complexed with 4b . The line is described by the equation $r(\text{Se}-\text{N}) = (1.9673(34) - 0.035(10) \times \sigma_X)$ Å ($R^2 = 0.7260$) and $r(\text{Se}-\text{N}) = (2.397(77) - 0.13(2) \times \sigma_X)$ Å ($R^2 = 0.8708$).	24
2.6	Solid state IR spectrum of 1k ·DMAP. The spectrum of the pure 1k is shown in gray.	25
2.7	Contributing resonance form of a Ch-bonded complex with strong Lewis bases. The double bond character of the carbonyl is decreased.	26
2.8	Single crystal x-ray structure of 1j ·DMAP, displaying the two systems in the asymmetric unit.	27
2.9	Calculated vs measured powder diffraction pattern for 1j ·DMAP.	27
2.10	29
2.11	Solid state ¹³ C-NMR spectrum of 1j ·DMAP (blue) overlaid on solution spectrum of the same (black). Signals are assigned according to the numbering scheme above.	30
2.12	Solid state ⁷⁷ Se-NMR spectrum of 1j ·DMAP. The primary resonances are visible at 834.69 and 867.02 ppm. The remaining peaks are spinning sidebands, and are separated from the parent signals by multiples of 10 kHz (the magic angle spinning frequency).	31

2.13 Proton decoupled solid state ^{31}P spectra of barium diethyl phosphate spinning at the magic angle, at the speed specified. The isotropic chemical shift is shown by the vertical dotted line.	31
2.14 Characteristic solid-state NMR powder lineshape for an asymmetric tensor e.g. in an alkene. The positions of the three principal values are shown.	32
2.15	33
2.16 Calculated chemical shielding tensor for 1a ·DMAP.	35
2.17 Single crystal of 1a ·DMAP used for SS-NMR.	35
2.18	36
2.19 NMR titration binding isotherms	39
2.20 Hammett plot of binding energies between ebselen derivatives and DMAP, determined by ^{77}Se -NMR titration. The line is described by the equation $\Delta G = (0.88(21) + 1.86(57) \times \sigma_X) \text{ kcal} \cdot \text{mol}^{-1}$ ($R^2 = 0.8437$).	40
2.21 Positive mode ESI of 1a ·DMAP·H $^+$	41
2.22 Negative mode ESI of 1a ·isonicotinate	41
2.23 TCID experiment of 1a ·isonicotinate	42

List of Tables

1.1	Selected structural parameters of Ch-bonded complexes	5
1.2	Hydrogen bond basicities of bases studied.	9
2.1	Selected structural and electron density parameters of Ch-bonded complexes.	21
2.2	Principal values of the chemical shift tensor extracted from powder spectra in Figure 2.15.	32
2.3	Principal values of the chemical shielding tensor calculated from optimised structures.	34
2.4	NMR titration binding energies	38

Abbreviations

LAH List Abbreviations Here

Constants

Speed of Light c = $2.997\ 924\ 58 \times 10^8$ ms⁻¹ (exact)

Symbols

a	distance	m
P	power	$\text{W} (\text{Js}^{-1})$
ω	angular frequency	rads^{-1}

Part I

The strength and nature of chalcogen bonding

Chapter 1

New insights into chalcogen bonding provided by co-crystal structures of benzisoselenazolinone derivatives and nitrogen bases.

This chapter was published in Cryst. Eng. Comm., 22 Jan 2019.^{1 *}

1.1 Abstract

A number of derivatives of benzisoselenazolinones, including the drug ebselen, have been synthesized, and their interactions with various nitrogen bases characterized through x-ray crystallography. Structural studies revealed a strong interaction in all cases, with Se···N distances well within the Van der Waals radii of the constituent atoms. We suggest that there is a significant charge transfer component to this interaction, in contrast to some other interactions of similar strength and directionality. We have also found that this interaction can be enhanced *via* H-bonding to the carbonyl group of the benzisoselenazolinone moiety.

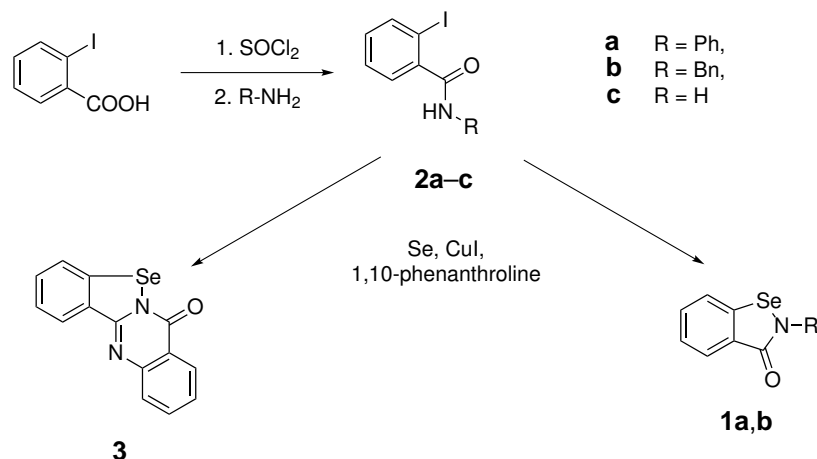
*Compound numbering, section headings, and terminology have been updated to fit this thesis.

1.2 Introduction

Chalcogen bonding (Ch-bonding) is a class of non-covalent interaction which has recently piqued the interests of the chemical community, and potential applications in materials and medicinal chemistry are emerging.^{2–5} It bears similarities to the related concept of halogen bonding, and the ubiquitous phenomenon of hydrogen bonding, in that the result is a relatively strong and highly directional non-bonded interaction.⁶ This strength and directionality has been exploited in crystal engineering,^{7–9} anion recognition,^{10–12} and bond activation,^{13–15} and appears to play a critical role in protein folding.^{16,17} Studies on Te···N Ch-bonds in solution phase have shown they can be as strong as 2.7 kcal/mol.¹⁸ A number of interesting and potentially useful supramolecular polymers have been synthesised and characterised by Vargas-Baca *et al.*, based on tellurium- and selenium-containing heterocycles.^{19,20}

In our efforts to apply the concept of Ch-bonding to biological systems, we turned to the benzisoselenazolinone scaffold of the antioxidant compound ebselen **1a**. **1a** has been known since the 1980s to effectively scavenge reactive oxygen species *in vivo*.²¹ It has remarkably low toxicity for an organoselenium compound, and is being investigated as a possible treatment for a number of conditions.^{22–25} It is also an ideal scaffold for Ch-bonding, bearing a selenium atom bonded to an electronegative amide nitrogen. Indeed, Ch-bonding in **1a** has been investigated previously in the context of crystal packing of the pure compound, but there is a lack of experimental evidence for interactions with other acceptors.²⁶

Numerous studies have examined the nature of the Ch-bond, in particular the balance between electrostatic effects (due to anisotropic electrostatic potential around the chalcogen atom), covalent (orbital overlap and electron delocalisation), and dispersion forces.^{27–31} In the case of halogen bonding, these contributions are generally well characterized. Halogen bonds range from primarily electrostatic (as in the case of fluorinated iodobenzenes³²) to charge-transfer dominated (molecular halogens³³). In the case of Ch-bonding in derivatives of **1a**, the contributions are less clear. We therefore sought to characterize Ch-bonding interactions between a number of derivatives of **1a**, and a variety of Ch-bond acceptors.

FIGURE 1.1: Synthesis of Ch-bond donors **1a**, **1b** and **3**.

1.3 Results and Discussion

1.3.1 Synthesis of benzisoselenazolone derivatives **1a** and **1b**

Compounds **1a** and **1b** were synthesized via published procedures from amides **2a** and **2b**.³⁴ The Se-tetracycle **3** was isolated in poor yield as the major product from the cyclization of primary amide **2c** in an attempt to form **1c**. It is noteworthy that the spectral characteristics of **3** are essentially identical to reported spectral data of **1c**.³⁴

TABLE 1.1: Selected structural parameters of Ch-bonded complexes

Complex	r(N···Se) Å	r(Se–N ₁) Å	r(Se–C ₁) Å	r(N ₁ –C(O)) Å	∠(N···Se–N ₁) °	∠(C _{para} ···N···Se) °
1a only	—					
1a · DMAP	2.371(1)	1.9676(10)	1.8959(12)	1.2345(14)	174.18(4)	173.52(4)
1b only	—	1.8805(14)	1.8867(16)	1.350(2)	—	—
1b · DMAP M1	2.4276(14)	1.9297(13)	1.8984(15)	1.348(2)	173.93(5)	174.89(5)
1b · DMAP M2	2.4331(14)	1.9191(14)	1.8966(14)	1.349(2)	175.30(5)	158.14(5)
1b · DMAP · H ₂ O	2.4046(15)	1.9367(14)	1.9070(14)	1.330(2)	175.54(5)	167.43(5)
1b · quinuclidine	2.5874(17)	1.9077(17)	1.898(2)	1.354(3)	176.77(7)	161.32(7)
1b · DABCO	2.6166(15)	1.9019(14)	1.8967(17)	1.355(2)	175.76(6)	160.00(6)
3 only	—	1.883(2)	1.899(3)	1.393(3)	—	—
3 · pyridine	2.461(3)	1.926(2)	1.908(3)	1.373(4)	174.13(9)	169.1(1)
3 · DMAP	2.304(1)	1.9716(9)	1.918(1)	1.375(1)	173.81(4)	173.16(4)

1.4 Co-crystal structures of benzisoselenazolinones and Lewis bases

High quality low temperature crystal structures were obtained for the parent benzisoselenazolinone derivatives **1a**,²⁶ **1b** and the Se-tetracycle **3** and the chalcogen-bonded co-crystals of

these compounds with a variety of nitrogen bases, including pyridine, dimethylaminopyridine (DMAP) quinuclidine and DABCO. Powder diffraction patterns were obtained of the bulk co-crystal material and compared with the single crystal data, with excellent agreement. This provides strong evidence of phase purity, with the exception of **1b**·DMAP, which indicated the presence of the unbound monomers in addition to the Ch-bonded adduct. Relevant structural parameters are presented in [Table 1.1](#), while all thermal ellipsoid plots are presented in the supplementary material (SUPP-Figures 7–15[†]). In the following discussion we begin by assessing the Ch-bond donor abilities of **1a**, **1b**, and **3** by comparing the structural parameters with a common nitrogen base adduct (DMAP), followed by comparison of a single Ch-bond donor **3** with two different nitrogen bases with markedly different basicities (pyridine and DMAP).

1.4.1 Effects of the benzisoselenazolone on Ch-bond strength

The DMAP adducts of **1a**, **1b** and **3** are characterized by near linear N···Se–N(CO) angles ([Table 1.1](#)) with N_{DMAP}···Se distances which are 2.4276(14) and 2.4331(16) Å for the two independent molecules of **1b**, 2.371(1) Å for **1a**, and the strikingly short N···Se distance of 2.304(1) Å for **3**. All are well within the van der Waals radii of N and Se of 3.85 Å.³⁵ The antipodal Se–N₁ bond distance within these adducts is significantly lengthened compared to the free Ch-bond donors, 0.063 Å in **1a**, 0.049 Å in **1b**, and 0.088 Å in **3**, with the degree of lengthening being related in an inverse sense to the N_{DMAP}···Se distance, in all cases the (non-antipodal) Se–C₁ bond is essentially unchanged. These structural parameters suggest an order of Ch-bond donor abilities **1b** < **1a** < **3**, which is supported by theoretical calculations which are discussed below, as well as being consistent with the ⁷⁷Se NMR chemical shifts.

1.4.2 Endocyclic bond lengthening associated with stronger complexes

Further discussion is warranted on the **1b**·DMAP adduct; firstly, the two independent molecules of **1b**·DMAP differ significantly with respect to the direction that the nitrogen base lone pair makes with the Se–N₁ bond; in molecule 1 this angle is close to colinear at 174.89(5)[°] while in molecule 2, this deviates significantly from linearity 158.14(5)[°]. Associated with this difference is a slightly longer N_{DMAP}···Se distance of 2.4331(14) Å in molecule 2 compared to 2.4276(14) Å in molecule 1 ($\Delta=0.0055$ Å; 3σ) and a shorter Se–N₁ distance 1.9191(14) Å vs 1.9297(14) Å ($\Delta=-0.10$ Å; 7.5σ) indicating a slightly weaker interaction. This can be seen in [Figure 1.2](#).

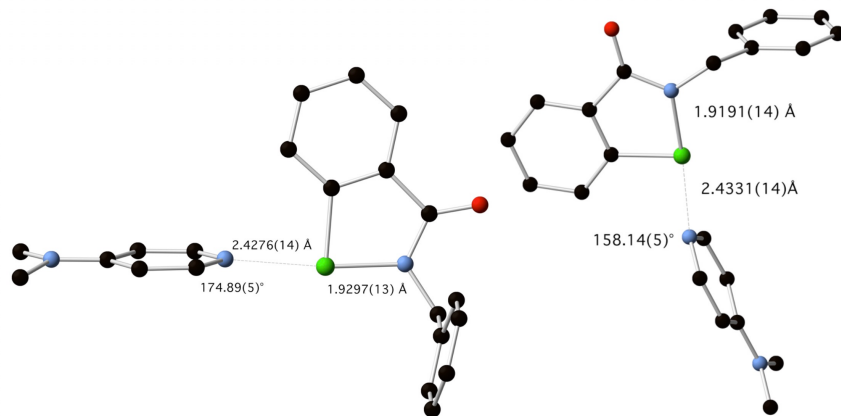


FIGURE 1.2: Structure of **1b**·DMAP, showing the two distinct geometries.

The structural effects described, particularly the lengthening of the Se–N₁ bond are consistent with donation of electron density from the nitrogen lone pair into the Se–N₁ antibonding orbital being a significant component of these N···Se Ch-bonds, which has been described before.²⁸

1.4.3 H-bond enhanced Ch-bonding

The second reason for further discussion of the **1b**·DMAP adduct is based on the structural parameters obtained for the hydrate structure **1b**·DMAP·H₂O which was serendipitously obtained by evaporation of a THF solution in an open flask. The structure is shown in Figure 1.3.

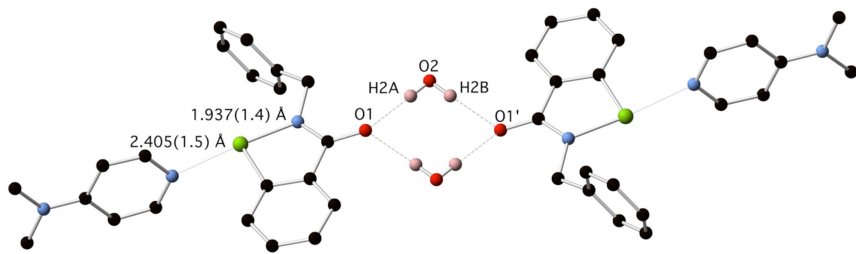


FIGURE 1.3: Structure of **1b**·DMAP·H₂O.

1b·DMAP·H₂O crystallizes as a centrosymmetric hydrogen-bonded dimer in which two water molecules bridge two molecules of **1b** across a crystallographic inversion centre. Of note, when comparison is made between the structural parameters for **1b**·DMAP molecule 1, which

has a similar geometry about the N···Se moiety as for **1b**·DMAP·H₂O, there is a significant contraction of the N_{DMAP}···Se distance from 2.4276(14) Å to 2.4046(14) Å ($\Delta=-0.023$ Å; 16 σ), and an increase in the Se–N₁ bond distance from 1.9297(13) to 1.9367(14) Å ($\Delta=0.007$ Å; 5 σ). We have coined the term ‘hydrogen-bond enhanced Ch-bonding’ to describe this interesting structural effect.

1.4.4 Effects of the Lewis base on Ch-bond strength

We were fortunate to obtain crystal structures of the Se-tetracycle **3** with both pyridine and DMAP, which gave us the opportunity to compare the structural effects arising from two Ch-bond acceptors with significantly different basicities. The pyridine adduct of **3** is characterized by a N_{PYR}···Se distance 2.461(3) Å and Se–N₁ distance of 1.926(2) Å and a near linear N_{PYR}···Se–N₁ angle, the Se–N₁ bond distance is significantly longer than the corresponding distance 1.883(2) Å in non-bound structure of **3**. The DMAP adduct of **3** is characterized by a significantly shorter N_{DMAP}···Se distance of 2.304(1) Å ($\Delta=-0.157$ Å) and longer Se–N₁ distance of 1.9716(9) Å ($\Delta=0.046$ Å), consistent with a significantly stronger interaction.

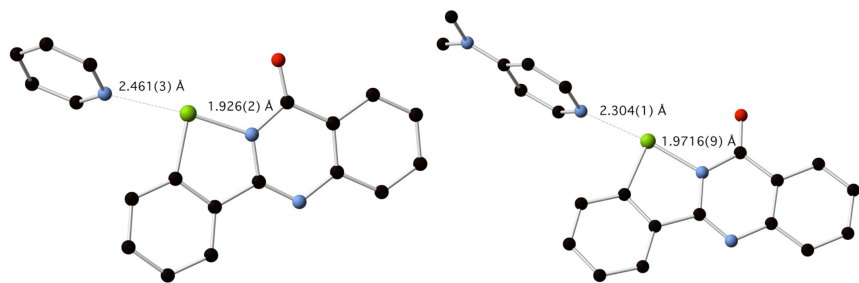


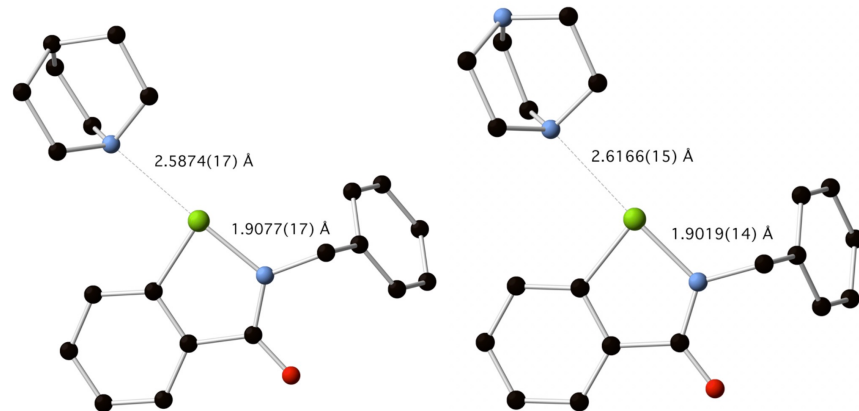
FIGURE 1.4: Pyridine and DMAP adducts of Se-tetracycle **3**.

Ch-bonded co-crystals of the benziselenazolinone derivative **1b** with the tertiary amines; quinuclidine and DABCO were obtained and structurally characterized. The adducts are presented in [Figure 1.5](#). The N_{QUIN}···Se and N_{DABCO}···Se distances of 2.5874(17) Å and 2.6166(15) Å for **1b**·quinuclidine and **1b**·DABCO respectively are significantly longer than those observed for **1b**·DMAP suggesting an order of Ch-bond strengths with **1b** DABCO < Quinuclidine < DMAP which correlates well with the hydrogen bond acceptor ability of these bases, as quantified by the pK_{HB} ([Table 1.2](#)).

TABLE 1.2: Hydrogen bond basicities of bases studied.

	pyridine	DABCO	quinuclidine	DMAP
pK _{HB}	1.86 ³⁶	2.63 ³⁷	2.71 ³⁷	2.80 ³⁶
1b ·base r(N···Se) / Å	—	2.6166(15)	2.5874(17)	2.4276(14) ^a
1b ·base ΔH _f / kcal/mol	-6.35	-7.82	—	-7.91

^aBond distance given is the shorter of the two coordination environments.

FIGURE 1.5: Adducts of benzisoselenazolinone **1b** with quinuclidine and DABCO.

1.4.5 DFT interaction energies, NBO and NEDA analysis

Interaction energies for the complexes were calculated using the ω B97X-D dispersion corrected functional, which has been used to study similar systems with good agreement with coupled cluster methods.²⁷ All geometries were therefore optimized at ω B97X-D/def2TZVP, and minima verified by frequency analysis.

NBO analysis was conducted on the optimized geometries, which supports our suggestion that there is a strong orbital component to Ch-bonding in these systems. Second order perturbation theory revealed that the energy associated with $n(N_{\text{base}}) \rightarrow \sigma^*(N_1-\text{Se})$ delocalization was 12.79, 15.45, and 16.23 kcal/mol for **1b**·DMAP, **1a**·DMAP, and **3**·DMAP respectively.

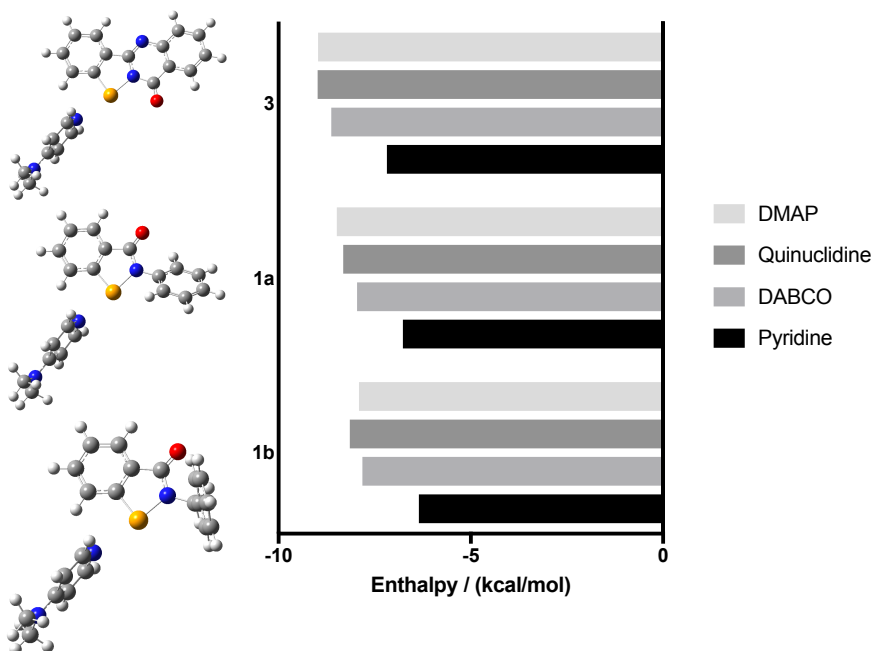


FIGURE 1.6: Interaction enthalpies calculated at ω B97X-D/def2TZVP. Optimised geometries for the DMAP complexes are shown to the left.

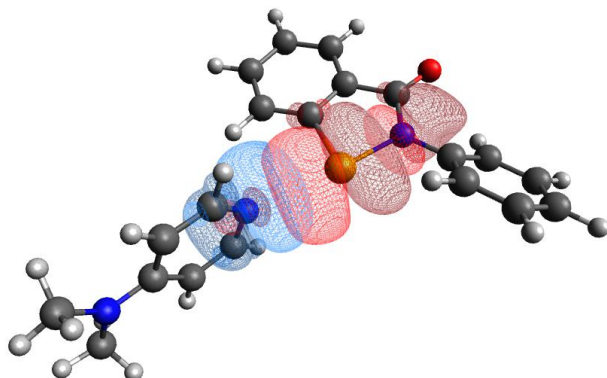


FIGURE 1.7: Overlap of nitrogen lone pair with σ^* (Se - N) in **1a**-DMAP complex.

1.5 Conclusion

In summary, we have demonstrated the importance of Ch-bonding between derivatives of ebselen **1a** and a variety of nitrogen bases. These selenium-containing heterocycles form close contacts with electron pair donors, well within the Van der Waals radii, with predictable geometries consistent with the Ch-bonding model. These interactions appear to be primarily due to orbital overlap as opposed to electrostatic or dispersion mediated effects, as evidenced by lengthening of the antipodal Se–N bond, and computational analysis, which is consistent

with findings in related systems by Cockcroft *et al.*²⁸ We have also found that the strength of a Ch-bond can be enhanced *via* a hydrogen bond to the carbonyl group of the heterocycle. We hope to exploit the strength and directionality of Ch-bonds in ebselen to target biomolecules such as nucleic acids and proteins using compounds containing the isoselenazolone moiety.

1.6 Supplementary materials

1.6.1 Synthetic procedures

1.6.1.1 Preparation of 2-phenylbenzo[*d*][1,2]selenazol-3(2*H*)-one **1a**.

Copper iodide (98.4 mg, 0.517 mmol) and 1,10-phenanthroline (83.1 mg, 0.461 mmol) were stirred in anhydrous DMF (3 mL) for 15 mins at r.t., then 2-iodo-N-phenylbenzamide (653.2 mg, 2.021 mmol), selenium (196.9 mg, 2.495 mmol) and potassium carbonate (627.3 mg, 4.539 mmol) were added sequentially under a flow of argon. The mixture was heated at 110°C for 8 h, when TLC showed consumption of starting material. The mixture was then tipped into brine (30 mL) and stirred to form a brown precipitate, which was extracted into DCM (40 mL) and washed with water (2 × 20 mL). The DCM solution was filtered through a silica plug, then evaporated, and the residue applied to a SNAP 25 g silica cartridge, eluting with a petroleum ether/ethyl acetate gradient. The major peak was evaporated to afford colourless crystals of **1a** (378.8 mg, 69%, m.p. 179.1–180.3°C, lit. mp 180–181°C). ⁷⁷Se NMR δ 959.66.

1.6.1.2 Preparation of 2-benzylbenzo[*d*][1,2]selenazol-3(2*H*)-one **1b**.

Copper iodide (95.8 mg, 0.503 mmol) and 1,10-phenanthroline (93.8 mg, 0.521 mmol) were stirred in anhydrous DMF (3 mL) for 15 mins at r.t., then N-benzyl-2-iodobenzamide (860.9 mg, 2.553 mmol), selenium (256.6 mg, 3.249 mmol) and potassium carbonate (542.2 mg, 3.923 mmol) were added sequentially under a flow of argon. The mixture was heated at 110°C for 5 h, when TLC showed consumption of starting material. The mixture was then tipped into brine (30 mL) and stirred to form a solid mass, which was dissolved in DCM (40 mL) and washed with water (2 × 20 mL). The DCM solution was filtered through a silica plug, then evaporated, and the residue applied to a SNAP 50 g silica cartridge, eluting with a petroleum ether/ethyl acetate gradient. The major peak was evaporated to afford pale yellow crystals of **1b** (396.4 mg, 53%, m.p. 137.8–138.8°C). ⁷⁷Se NMR δ 884.02.

1.6.1.3 Preparation of 5*H*-benzo[4,5][1,2]selenazolo[2,3-*a*]quinazolin-5-one **3**.

Copper iodide (96.4 mg, 0.503 mmol) and 1,10-phenanthroline (85.7 mg, 0.476 mmol) were stirred in anhydrous DMF (4 mL) for 10 mins at r.t., then 2-iodobenzamide (510.6 mg, 2.067 mmol), selenium (209.5 mg, 2.653 mmol) and potassium carbonate (506.3 mg, 3.663 mmol) were added sequentially under a flow of argon. The mixture was heated at 110°C for 12 h, when TLC showed consumption of starting material. The mixture was then tipped into brine (30 mL) and stirred to form a solid mass, which was extracted into ethyl acetate (20 mL) and washed with water (2 × 20 mL). The DCM solution was filtered through a silica plug, then evaporated, and the residue applied to a SNAP 50 g silica cartridge, eluting with a petroleum ether/ethyl acetate gradient. The major peak was evaporated to afford pale yellow crystals of **3** (45.8 mg, 15%, m.p. 267–268°C). ⁷⁷Se NMR δ 992.48.

1.6.2 Crystallographic data

Intensity data was collected on an Oxford Diffraction SuperNova CCD diffractometer using either Cu-K α or Mo-K α radiation at 130.0(1) K, or on a Rigaku XtalLAB Synergy at 100.0(1) K. Compound **1b**·DMAP·H₂O underwent a destructive phase change when cooling to 130 K, therefore data were collected at 200 K. Data for **3** was collected on the MX1 beamline at the Australian Synchrotron.³⁸ The temperature was maintained using an Oxford Cryostream cooling device. The structures were solved by direct methods and difference Fourier synthesis.³⁹ Thermal ellipsoid plot was generated using the program ORTEP-3⁴⁰ integrated within the WINGX⁴¹ suite of programs.

1.6.2.1 Crystal data for **1a**·DMAP

C₂₀H₁₉N₃OSe, $M = 396.34$, $T = 130.0$ K, $\lambda = 0.71073$ Å, Triclinic, space group P $\bar{1}$, $a = 8.3674(3)$, $b = 9.8399(5)$, $c = 10.6622(5)$ Å, $\alpha = 93.296(4)$ °, $\beta = 93.021(4)$ °, $\gamma = 101.210(4)$ °, $V = 857.86(7)$ Å³, $Z = 2$. $D_c = 1.534$ mg M⁻³, $\mu(\text{Mo-K}\alpha) = 2.201$ mm⁻¹, $F(000) = 404$, crystal size 0.52 × 0.34 × 0.23 mm. 11339 reflections measured, $\theta_{\max} = 36.66$ °, 7889 independent reflections, $R_{\text{int}} = 0.0163$, the final R was 0.0293 ($I > 2\theta(I)$, 6882 reflections) and $wR(F^2)$ was 0.0721 (all data), GOF 0.992. CCDC 1867205. From dichloromethane/pentane (70%) m.p. 111.3–112.1°C.

1.6.2.2 Crystal data for **1b**

$C_{14}H_{11}NOSe$, $M = 288.20$, $T = 100.0$ K, $\lambda = 0.71073$ Å, Orthorhombic, space group $Pca2_1$, $a = 11.7848(3)$, $b = 4.5869(1)$, $c = 21.3572(5)$ Å, $V = 1154.48(5)$ Å³, $Z = 4$. $D_c = 1.658$ mg M⁻³, $\mu(\text{Mo-K}\alpha) = 3.233$ mm⁻¹, $F(000) = 576$, crystal size $0.63 \times 0.54 \times 0.22$ mm. 44918 reflections measured, $\theta_{\max} = 45.38^\circ$, 9588 independent reflections, $R_{\text{int}} = 0.0481$, the final R was 0.0331 ($I > 2\theta(I)$, 7848 reflections) and $wR(F^2)$ was 0.0792 (all data), GOF 1.063. CCDC 1867211.

1.6.2.3 Crystal data for **1b·DMAP·H₂O**

$C_{21}H_{21}N_3OSe \cdot (H_2O)$, $M = 428.38$, $T = 200.0$ K, $\lambda = 0.71073$ Å, Triclinic, space group $P\bar{1}$, $a = 9.6254(2)$, $b = 10.2486(2)$, $c = 10.6505(2)$ Å, $\alpha = 83.660(2)^\circ$, $\beta = 76.398(2)^\circ$, $\gamma = 78.423(2)^\circ$, $V = 998.19(4)$ Å³, $Z = 2$. $D_c = 125$ mg M⁻³, $\mu(\text{Mo-K}\alpha) = 1.901$ mm⁻¹, $F(000) = 440$, crystal size $0.41 \times 0.32 \times 0.23$ mm. 30047 reflections measured, $\theta_{\max} = 41.06^\circ$, 12528 independent reflections, $R_{\text{int}} = 0.0267$, the final R was 0.0456 ($I > 2\theta(I)$, 6303 reflections) and $wR(F^2)$ was 0.1219 (all data), GOF 1.000. CCDC 1867213. From THF in an open flask (90%) m.p. 96–97°C.

1.6.2.4 Crystal data for **1b·DMAP**

$C_{21}H_{21}N_3OSe$, $M = 410.37$, $T = 130.0$ K, $\lambda = 0.71073$ Å, Triclinic, space group $P\bar{1}$, $a = 9.6002(4)$, $b = 10.2109(4)$, $c = 19.8380(7)$ Å, $\alpha = 78.710(3)^\circ$, $\beta = 84.901(3)^\circ$, $\gamma = 77.458(4)^\circ$, $V = 1859.33(13)$ Å³, $Z = 4$, $Z' = 2$. $D_c = 1.466$ mg M⁻³, $\mu(\text{Mo-K}\alpha) = 2.034$ mm⁻¹, $F(000) = 840$, crystal size $0.65 \times 0.24 \times 0.37$ mm. 36541 reflections measured, $\theta_{\max} = 40.95^\circ$, 23437 independent reflections, $R_{\text{int}} = 0.0264$, the final R was 0.0448 ($I > 2\theta(I)$, 15177 reflections) and $wR(F^2)$ was 0.1120 (all data), GOF 1.044. CCDC 1867209. From dichloromethane/pentane (60%) m.p. 86.1–92.5°C.

1.6.2.5 Crystal data for **1b·quinuclidine**

$C_{21}H_{24}N_2OSe$, $M = 399.38$, $T = 130.0$ K, $\lambda = 1.54184$ Å, Monoclinic, space group $P2_1/c$, $a = 10.1610(2)$, $b = 16.0506(3)$, $c = 11.4300(2)$ Å, $\beta = 104.622(2)^\circ$, $V = 1803.75(6)$ Å³, $Z = 4$. $D_c = 1.471$ mg M⁻³, $\mu(\text{Cu-K}\alpha) = 3.895$ mm⁻¹, $F(000) = 824$, crystal size $0.29 \times 0.10 \times 0.03$ mm. 12588 reflections measured, $\theta_{\max} = 77.19^\circ$, 3771 independent reflections, $R_{\text{int}} = 0.0379$, the final R

was 0.0329 ($I > 2\theta(I)$, 3397 reflections) and $wR(F^2)$ was 0.0849 (all data), GOF 1.028. CCDC 1867207. From dichloromethane/pentane (50%) m.p. 135.2–137.4°C.

1.6.2.6 Crystal data for 1b·DABCO

$C_{20}H_{23}N_3OSe$, $M = 400.37$, $T = 130.0$ K, $\lambda = 1.54184$ Å, Monoclinic, space group $P2_1/c$, $a = 10.1249(2)$, $b = 15.9246(3)$, $c = 11.4660(2)$ Å, $\beta = 106.572(2)$ °, $V = 1771.93(6)$ Å³, $Z = 4$. $D_c = 1.501$ mg M⁻³, $\mu(\text{Cu-K}\alpha) = 2.965$ mm⁻¹, $F(000) = 824$, crystal size $0.37 \times 0.17 \times 0.04$ mm. 13121 reflections measured, $\theta_{\max} = 77.12$ °, 3711 independent reflections, $R_{\text{int}} = 0.0280$, the final R was 0.0258 ($I > 2\theta(I)$, 3333 reflections) and $wR(F^2)$ was 0.0657 (all data), GOF 1.056. CCDC 1867206. From dichloromethane/pentane (65%) m.p. 131.4–133.3°C.

1.6.2.7 Crystal data for 3

$C_{14}H_8N_2OSe$, $M = 299.18$, $T = 100.0$ K, $\lambda = 0.71092$ Å, Orthorhombic, space group $Pca2_1$, $a = 17.371(4)$, $b = 5.3080(11)$, $c = 11.633(2)$ Å, $V = 1072.6(4)$ Å³, $Z = 4$. $D_c = 1.853$ mg M⁻³, $\mu(\text{Mo-K}\alpha) = 3.486$ mm⁻¹, $F(000) = 592$, crystal size $0.15 \times 0.10 \times 0.02$ mm. 16031 reflections measured, $\theta_{\max} = 31.56$ °, 2967 independent reflections, $R_{\text{int}} = 0.0363$, the final R was 0.0271 ($I > 2\theta(I)$, 2061 reflections) and $wR(F^2)$ was 0.0751 (all data), GOF 1.129. CCDC 1867208.

1.6.2.8 Crystal data for 3·pyridine

$C_{19}H_{13}N_3OSe$, $M = 378.28$, $T = 130.0$ K, $\lambda = 1.54184$ Å, Monoclinic, space group $P2_1/c$, $a = 20.7476(9)$, $b = 4.9407(2)$, $c = 17.6687(7)$ Å, $\beta = 107.376(4)$ °, $V = 1156.27(5)$ Å³, $Z = 4$. $D_c = 1.454$ mg M⁻³, $\mu(\text{Cu-K}\alpha) = 3.018$ mm⁻¹, $F(000) = 760$, crystal size $0.56 \times 0.05 \times 0.03$ mm. 5766 reflections measured, $\theta_{\max} = 75.76$ °, 3419 independent reflections, $R_{\text{int}} = 0.0301$, the final R was 0.0346 ($I > 2\theta(I)$, 2889 reflections) and $wR(F^2)$ was 0.0955 (all data), GOF 1.054. CCDC 1867211. From dichloromethane/pentane (70%) m.p. 247.5–248.4°C.

1.6.2.9 Crystal data for 3·DMAP

$C_{21}H_{18}N_4OSe$, $M = 421.35$, $T = 100.0$ K, $\lambda = 0.71073$ Å, Triclinic, space group $P\bar{1}$, $a = 8.8093(2)$, $b = 10.7445(2)$, $c = 10.9812(2)$ Å, $\alpha = 111.687(2)$ °, $\beta = 109.283(2)$ °, $\gamma = 96.631(2)$ °, $V = 877.57(3)$ Å³, $Z = 2$, $Z' = 2$. $D_c = 1.595$ mg M⁻³, $\mu(\text{Mo-K}\alpha) = 2.159$ mm⁻¹, $F(000) = 428$, crystal size

$0.18 \times 0.11 \times 0.06$ mm. 56053 reflections measured, $\theta_{\max} = 41.07^\circ$, 11273 independent reflections, $R_{\text{int}} = 0.0547$, the final R was 0.0358 ($I > 2\theta(I)$, 8667 reflections) and $wR(F^2)$ was 0.0872 (all data), GOF 1.048. CCDC 1867212. From dichloromethane/pentane (80%) m.p. 248.8–249.4°C.

References

- (1) Fellowes, T.; White, J. M. *CrystEngComm* **2019**, *21*, 1539–1542.
- (2) Mitchell, M. O. *Journal of Molecular Modeling* **2017**, *23*, 287.
- (3) Wonner, P.; Vogel, L.; Düser, M.; Gomes, L.; Kniep, F.; Mallick, B.; Werz, D. B.; Huber, S. M. *Angewandte Chemie International Edition* **2017**, *56*, 12009–12012.
- (4) Fanfrlík, J.; Přáda, A.; Padělková, Z.; Pecina, A.; Macháček, J.; Lepšík, M.; Holub, J.; Růžička, A.; Hnyk, D.; Hobza, P. *Angewandte Chemie - International Edition* **2014**, *53*, 10139–10142.
- (5) Vogel, L.; Wonner, P.; Huber, S. M. *Angewandte Chemie International Edition* **2019**, *58*, 1880–1891.
- (6) Paolo, T. D.; Sandorfy, C. *Canadian Journal of Chemistry* **1974**, *52*, 3612–3622.
- (7) Gleiter, R.; Werz, D. B.; Rausch, B. J. *Chemistry - A European Journal* **2003**, *9*, 2676–2683.
- (8) Kremer, A.; Fermi, A.; Biot, N.; Wouters, J.; Bonifazi, D. *Chemistry (Weinheim an der Bergstrasse, Germany)* **2016**, *22*, 5665–5675.
- (9) Huynh, H.-T.; Jeannin, O.; Fourmigué, M. *Chem. Commun.* **2017**, 8467–8469.
- (10) Lim, J. Y. C.; Marques, I.; Thompson, A. L.; Christensen, K. E.; Félix, V.; Beer, P. D. *Journal of the American Chemical Society* **2017**, *139*, 3122–3133.
- (11) Lim, J. Y. C.; Liew, J. Y.; Beer, P. D. *Chemistry - A European Journal* **2018**, DOI: [10.1002/chem.201803393](https://doi.org/10.1002/chem.201803393).
- (12) Garrett, G. E.; Carrera, E. I.; Seferos, D. S.; Taylor, M. S. *Chem. Commun.* **2016**, *52*, 9881–9884.
- (13) Wonner, P.; Vogel, L.; Kniep, F.; Huber, S. M. *Chemistry - A European Journal* **2017**, *23*, 16972–16975.
- (14) Benz, S.; López-Andarias, J.; Mareda, J.; Sakai, N.; Matile, S. *Angewandte Chemie International Edition* **2017**, *56*, 812–815.

- (15) Benz, S.; Mareda, J.; Besnard, C.; Sakai, N.; Matile, S. *Chemical Science* **2017**, *8*, 8164–8169.
- (16) Iwaoka, M.; Takemoto, S.; Okada, M.; Tomoda, S. *Chemistry Letters* **2001**, 132–133.
- (17) Iwaoka, M. In *Noncovalent Forces*, Scheiner, S., Ed.; Springer International Publishing: Cham, 2015, pp 265–289.
- (18) Garrett, G. E.; Gibson, G. L.; Straus, R. N.; Seferos, D. S.; Taylor, M. S. *Journal of the American Chemical Society* **2015**, *137*, 4126–4133.
- (19) Ho, P. C.; Szydlowski, P.; Sinclair, J.; Elder, P. J. W.; Kübel, J.; Gendy, C.; Lee, L. M.; Jenkins, H.; Britten, J. F.; Morim, D. R.; Vargas-Baca, I. *Nature Communications* **2016**, *7*, 11299.
- (20) Ho, P. C.; Rafique, J.; Lee, J.; Lee, L. M.; Jenkins, H. A.; Britten, J. F.; Braga, A. L.; Vargas-Baca, I. *Dalton Trans.* **2017**, *46*, 6570–6579.
- (21) Müller, A.; Cadenas, E.; Graf, P.; Sies, H. *Biochemical Pharmacology* **1984**, *33*, 3235–3239.
- (22) Schewe, T. *General Pharmacology* **1995**, *26*, 1153–1169.
- (23) Kil, J.; Pierce, C.; Tran, H.; Gu, R.; Lynch, E. D. *Hearing Research* **2007**, *226*, 44–51.
- (24) Singh, N.; Halliday, A. C.; Thomas, J. M.; Kuznetsova, O.; Baldwin, R.; Woon, E. C.; Aley, P. K.; Antoniadou, I.; Sharp, T.; Vasudevan, S. R.; Churchill, G. C. *Nature Communications* **2013**, *4*, 1332–1337.
- (25) Parnham, M.; Sies, H. *Expert Opinion on Investigational Drugs* **2000**, *9*, 607–619.
- (26) Thomas, S. P.; Satheeshkumar, K.; Mugesh, G.; Guruow, T. N. *Chemistry - A European Journal* **2015**, *21*, 6793–6800.
- (27) Oliveira, V.; Cremer, D.; Kraka, E. *Journal of Physical Chemistry A* **2017**, *121*, 6845–6862.
- (28) Pascoe, D. J.; Ling, K. B.; Cockroft, S. L. *Journal of the American Chemical Society* **2017**, *139*, 15160–15167.
- (29) De Vleeschouwer, E.; Denayer, M.; Pinter, B.; Geerlings, P.; De Proft, F. *Journal of Computational Chemistry* **2017**, 557–572.
- (30) Kolář, M. H.; Hobza, P. *Chemical Reviews* **2016**, *116*, 5155–5187.
- (31) Gleiter, R.; Haberhauer, G.; Werz, D. B.; Rominger, F.; Bleiholder, C. *Chemical Reviews* **2018**, *118*, 2010–2041.
- (32) Präsang, C.; Whitwood, A. C.; Bruce, D. W. *Crystal Growth and Design* **2009**, *9*, 5319–5326.
- (33) Mulliken, R. S. *Journal of the American Chemical Society* **1950**, *72*, 600–608.

- (34) Balkrishna, S. J.; Bhakuni, B. S.; Chopra, D.; Kumar, S. *Organic Letters* **2010**, *12*, 5394–5397.
- (35) Batsanov, S. S. *Inorganic Materials* **2001**, *37*, 871–885.
- (36) Berthelot, M.; Laurence, C.; Safar, M.; Besseau, F. *Journal of the Chemical Society, Perkin Transactions 2* **1998**, 283–290.
- (37) Graton, J.; Besseau, F.; Berthelot, M.; Raczynska, E. D.; Laurence, C. *Canadian Journal of Chemistry* **2002**, *80*, 1375–1385.
- (38) Cowieson, N. P.; Aragao, D.; Clift, M.; Ericsson, D. J.; Gee, C.; Harrop, S. J.; Mudie, N.; Panjikar, S.; Price, J. R.; Riboldi-Tunnicliffe, A.; Williamson, R.; Caradoc-Davies, T. *Journal of Synchrotron Radiation* **2015**, *22*, 187–190.
- (39) Sheldrick, G. M. *Acta Crystallographica Section C: Structural Chemistry* **2015**, *71*, 3–8.
- (40) Farrugia, L. J. *Journal of Applied Crystallography* **1997**, *30*, 565.
- (41) Farrugia, L. J. *Journal of Applied Crystallography* **1999**, *32*, 837–838.

Chapter 2

Further investigations into Ch-bonded complexes

2.1 Introduction

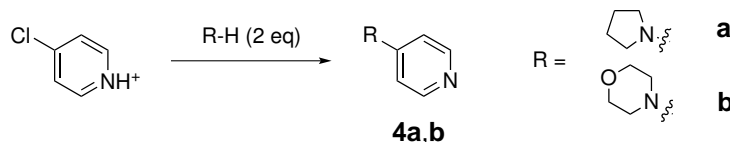
In the previous chapter, we established that Ch-bonding is not only present in ebselen derivatives, but dominates packing in crystals of the pure compound (through Se \cdots O interactions) and in co-crystals with a variety of Lewis bases. In this chapter, we extend our investigation to a wider range of derivatives with systematically varied electronic properties.

Linear free energy relationships are...

2.2 Results and discussion

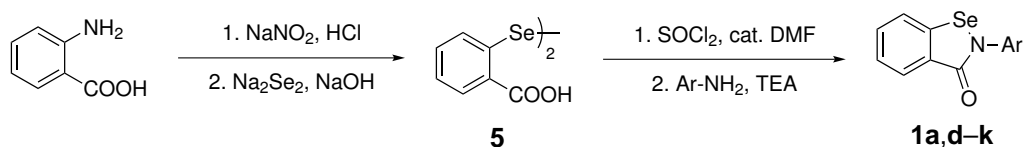
Our previous work had shown that electron-rich pyridines (specifically DMAP) formed the strongest Ch-bonds out of all the bases trialled. This is roughly consistent with the hydrogen bond basicity (pK_{HB}) of the bases (Table 1.2). Methyl cation affinities?¹ The planar geometry and aromatic character of DMAP may also facilitate crystallisation, as opposed to the relatively bulky and flexible aliphatic bases which may not pack as efficiently. For these reasons, we restricted the bases used in this study to other electron-rich pyridines. Although DMAP is already a very strong base, the basicity can be increased by incorporating the aniline nitrogen in another ring. This reduces the energetic penalty associated with the delocalisation of the

lone pair into the pyridine ring, by forcing a more planar geometry upon the nitrogen.^{2,3} Compounds **4a** and **4b** were therefore synthesised by treating 4-chloropyridine hydrochloride with 2 equivalents of the appropriate base ([Scheme 2.1](#)).



SCHEME 2.1: Synthesis of Lewis bases **4a** and **4b**.

The benzisoselenazolone derivatives **1a,d–k** were prepared by the reaction of substituted anilines with a selenenyl chloride intermediate **5**, ultimately derived from anthranilic acid ([Scheme 2.2](#)). The one-pot selenocyclisation reaction used in the previous work often did not tolerate the various functional groups on the aryl ring, affording reduction, cross-coupling, or protodehalogenation byproducts.



Compound	R =	Compound	R =	Compound	R =
1a	-H	1f	-CF ₃	1i	-CH ₃
1d	-NO ₂	1g	-Br	1j	-OMe
1e	-CN	1h	-CO ₂ Et	1k	-OEt

SCHEME 2.2: Synthesis of benzisoselenazolone derivatives **1a,d–k**.

Co-crystals of the benzisoselenazolones and pyridines were grown by vapour diffusion from an equimolar solution in dichloromethane/pentane. Relevant structural parameters are given in [Table 2.1](#). In addition to the structural parameters, we characterised the various Ch-bonds using Bader's QTAIM framework. Depending on the quality of the data we were able to obtain for each crystal, we used:

- experimental electron density from a multipole refinement with atomic coordinates determined from high angle refinement ($d < 0.8\text{\AA}$),
- experimental electron density from a multipole refinement with atomic coordinates determined by refinement using aspherical scattering factors derived from the DFT electron density,
- density derived from the DFT calculation.

The second “hybrid” strategy has the advantage of being able to capture electron density effects not fully described by DFT, while not requiring a large amount of weak high-angle (or neutron) data for the reliable determination of atomic coordinates. The low-angle data, however, does need to be free from faults, so this strategy may still not be appropriate for all data sets.

TABLE 2.1: Selected structural and electron density parameters of Ch-bonded complexes.

Complex	r(N···Se) Å	r(Se–N ₁) Å	r(Se–C ₁) Å	r(N ₁ –C(O)) Å	∠(N···Se–N ₁) °	∠(C _{para} ···N···Se) °	$\rho_{\text{BCP}}(\text{Se} \cdots \text{N})$ e/Å ³	$\nabla^2(\rho_{\text{BCP}})(\text{Se} \cdots \text{N})$ e/Å ⁵
1a	—	1.896(3)	1.892(4)	1.359(5)	—	—	—	—
1d	—	—	—	—	—	—	—	—
1e	—	1.894(2)	1.877(2)	1.372(2)	—	—	—	—
1f^a	—	1.880(9)	1.889(9)	1.38(1)	—	—	—	—
1f^b	—	1.898(8)	1.901(9)	1.37(1)	—	—	—	—
1g	—	1.898(2)	1.889(2)	1.371(3)	—	—	—	—
1h	—	1.902(2)	1.879(2)	1.371(3)	—	—	—	—
1i	—	1.904(3)	1.890(3)	1.365(4)	—	—	—	—
1j	—	1.8741(9)	1.887(1)	1.356(1)	—	—	—	—
1k	—	1.901(3)	1.885(4)	1.357(4)	—	—	—	—
1a-DMAP	2.371(1)	1.968(1)	1.896(1)	1.358(2)	174.18(4)	173.51(6)	0.3511	2.6960 ^c
1d-DMAP	2.2424(5)	2.0200(4)	1.9086(4)	1.3592(4)	173.57(2)	175.47(2)	0.5372	3.8680 ^c
1e-DMAP	2.301(1)	1.997(1)	1.899(2)	1.368(2)	174.79(5)	167.57(6)	0.4130	2.5210 ^c
1e-DMAP^{d,a}	2.254(2)	2.019(2)	1.902(1)	1.366(2)	174.46(6)	176.33(7)	0.4780	2.4816 ^e
1e-DMAP^{d,b}	2.308(2)	1.993(1)	1.901(1)	1.372(2)	174.93(5)	167.85(7)	0.4284	2.4558 ^e
1f-DMAP	2.3347(9)	1.9855(9)	1.899(1)	1.372(1)	175.24(4)	162.65(5)	0.4048	2.4112 ^e
1g-DMAP	2.3215(7)	1.9840(7)	1.9021(8)	1.362(1)	173.85(3)	173.56(4)	0.4058	3.1160
1h-DMAP^d	2.322(1)	1.982(1)	1.902(1)	1.367(2)	174.96(4)	172.86(6)	—	—
1i-DMAP	2.4301(4)	1.9341(4)	1.8918(4)	1.3650(6)	175.33(1)	158.64(2)	—	—
1j-DMAP^{f,a}	2.270(1)	1.9689(9)	1.899(1)	1.350(1)	174.17(3)	159.44(4)	—	—
1j-DMAP^{f,b}	2.4496(9)	1.9267(9)	1.895(1)	1.357(1)	174.57(3)	160.53(4)	—	—
1j-DMAP^{g,a}	2.334(1)	1.965(1)	1.894(1)	1.363(1)	175.95(5)	155.71(6)	—	—
1j-DMAP^{g,b}	2.407(1)	1.941(1)	1.894(1)	1.358(2)	176.12(5)	156.60(6)	—	—
1k-DMAP^a	2.517(2)	1.921(1)	1.895(2)	1.356(3)	172.30(6)	158.37(8)	—	—
1k-DMAP^b	2.327(5)	1.931(2)	1.894(2)	1.353(3)	171.4(1)	151.2(3)	—	—
1a-4a	2.350(1)	1.9830(9)	1.8985(7)	1.3616(8)	174.20(3)	176.46(4)	0.2419	5.4650
1d-4a	—	—	—	—	—	—	—	—
1e-4a	2.289(1)	2.000(1)	1.902(1)	1.363(2)	174.77(5)	175.06(7)	—	—
1f-4a	—	—	—	—	—	—	—	—
1g-4a	2.319(2)	1.981(2)	1.895(1)	1.362(2)	174.57(6)	174.60(8)	0.3617	3.7020
1h-4a	2.337(3)	1.982(3)	1.906(4)	1.374(5)	173.5(1)	170.1(2)	—	—
1i-4a	2.272(1)	1.986(1)	1.905(1)	1.351(2)	172.66(5)	173.51(6)	—	—
1j-4a	—	—	—	—	—	—	—	—
1k-4a^a	2.356(3)	1.972(3)	1.898(3)	1.355(4)	174.5(1)	170.2(1)	—	—
1k-4a^b	2.371(3)	1.964(3)	1.898(3)	1.360(4)	174.9(1)	170.9(1)	—	—
1a-4b^f	2.414(2)	1.960(2)	1.902(2)	1.366(2)	175.46(6)	166.23(8)	—	—
1a-4b^g	2.420(2)	1.967(2)	1.903(2)	1.363(2)	176.7(1)	174.23(8)	—	—
1d-4b	—	—	—	—	—	—	—	—
1e-4b^d	2.301(1)	1.993(1)	1.907(1)	1.368(2)	173.08(5)	164.75(6)	—	—
1f-4b	—	—	—	—	—	—	—	—
1g-4b	2.381(2)	1.975(2)	1.905(2)	1.367(2)	173.84(6)	174.97(8)	—	—
1h-4b	2.337(3)	1.982(3)	1.906(4)	1.374(5)	173.5(1)	170.1(2)	—	—
1i-4b	2.412(5)	1.977(5)	1.908(5)	1.360(7)	174.4(2)	178.9(2)	—	—
1j-4b	—	—	—	—	—	—	—	—
1k-4b^a	2.398(4)	1.958(4)	1.894(6)	1.367(6)	174.6(2)	174.1(2)	—	—
1k-4b^b	2.448(6)	1.951(4)	1.901(5)	1.367(5)	175.5(2)	170.5(3)	—	—

^aEnvironment *a*^bEnvironment *b*^cFully experimental density used^dDCM solvate^eDFT density used^fPolymorph 1^gPolymorph 2

2.2.1 Hammett plots of crystallographic data.

Evident in this data is a trend of increasing Ch-bond length with increasing electron donating character of the substituent. There are a number of methods to quantify this property of the substituent, and we will explore a couple of the most common. The Hammett substituent parameter σ for a given substituent is determined from the ionization equilibrium of the parent carboxylic acid. Although originally used to explain reaction *kinetics* with an associated reaction constant ρ , the substituent constant provides a convenient measure of electron donating character for ground state phenomena as well.⁴ Within the context of Ch-bonding, this can be rationalised by considering the approach of the Lewis base to form the Ch-bond as an incipient nucleophilic substitution at the selenium, and invoking the Hammond postulate to relate the transition state geometry to the ground state. Closely linked to the substituent constant σ are the values of σ^+ and σ^- , which can be used when mesomeric effects have a strong influence on the property being studied. Hammett substituent parameters are particularly convenient as they have been determined for a wide variety of substituents.

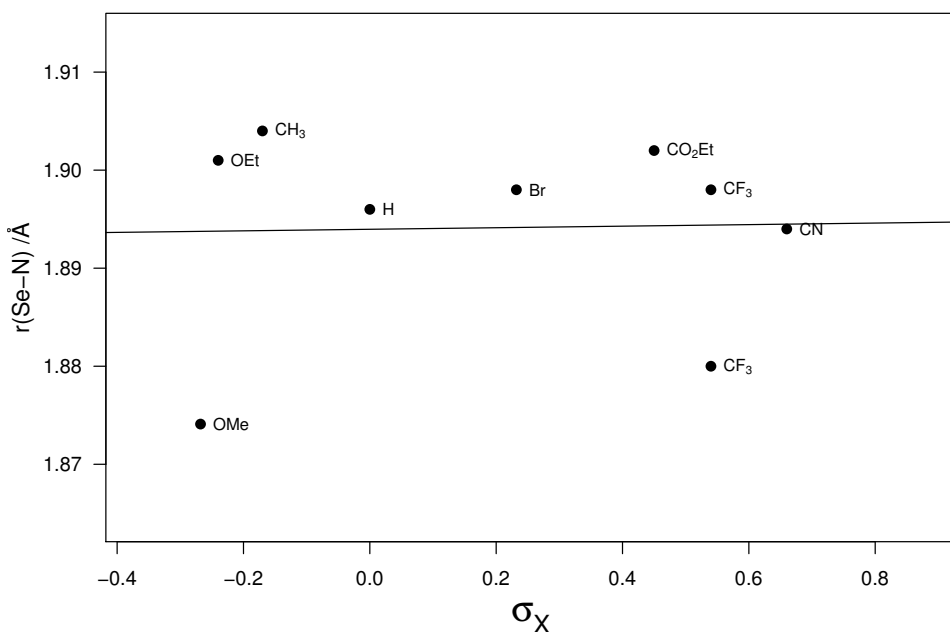


FIGURE 2.1: Hammett plot of endocyclic Se–N bond length of uncomplexed ebselen derivatives.

The structural effects most relevant to Ch-bonding will manifest themselves in the vicinity of the selenium atom. Of particular interest is the endocyclic Se–N bond length, which serves as

a measure of σ^* (Se–N) orbital occupancy, thus the degree of hyperconjugation and strength of the Ch-bond. As can be seen in [Figure 2.1](#), there is practically no correlation between the electronic properties of the aryl ring and the endocyclic Se–N bond length in crystals of the unbound ebselen derivatives. This is not unexpected, as in all cases the crystals consist of one dimensional chains of ebselen molecules Ch-bonded to the carbonyl oxygen of the next ([Figure 2.2](#)). As the magnitude of the σ -hole (Ch-bond donor ability) is *increased* by an electron withdrawing substituent, the Ch-bond acceptor ability of the carbonyl is *decreased*. These opposing effects appear to be approximately equal in magnitude, so cancel each other out and give a very flat and featureless Hammett plot.

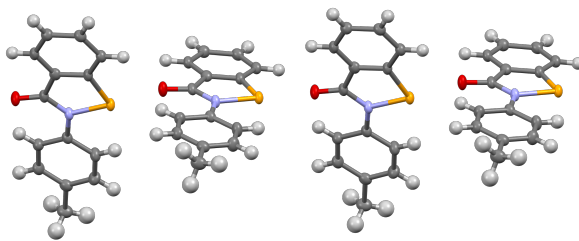


FIGURE 2.2: One dimensional chains formed by Ch-bonding between the selenium and carbonyl oxygen in **1i**. All other ebselen derivatives display a similar packing motif.

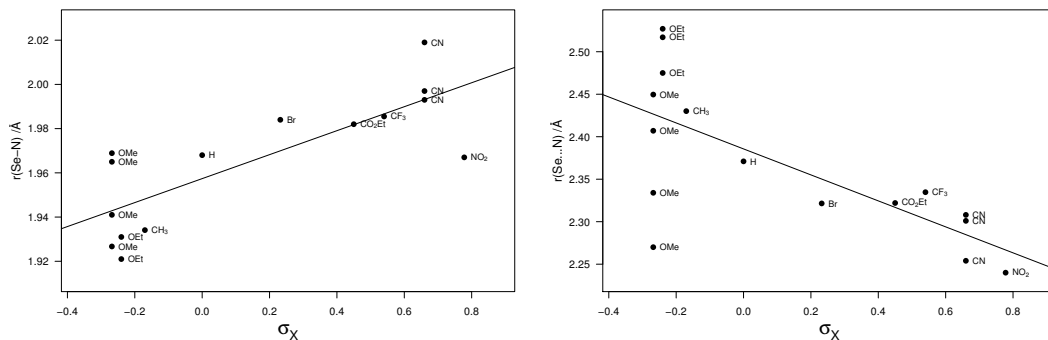


FIGURE 2.3: Hammett plots of endocyclic Se–N bond length and Se···N Ch-bond length of ebselen derivatives complexed with DMAP. The lines are described by the equations $r(\text{Se}-\text{N}) = (1.957(5) + 0.054(12) \times \sigma_X) \text{ \AA}$ and $r(\text{Se}\cdots\text{N}) = (2.385(17) - 0.15(4) \times \sigma_X) \text{ \AA}$.

Fortunately, inspecting the same bond length in co-crystals of ebselen derivatives and a Lewis base gives us a much clearer dependence, as can be seen in [Figure 2.3](#), [Figure 2.4](#), and [Figure 2.5](#). This is because the Ch-bond acceptor ability is now independent of the electronic properties of the Ch-bond donor, so the Se–N bond length is determined solely by the latter.

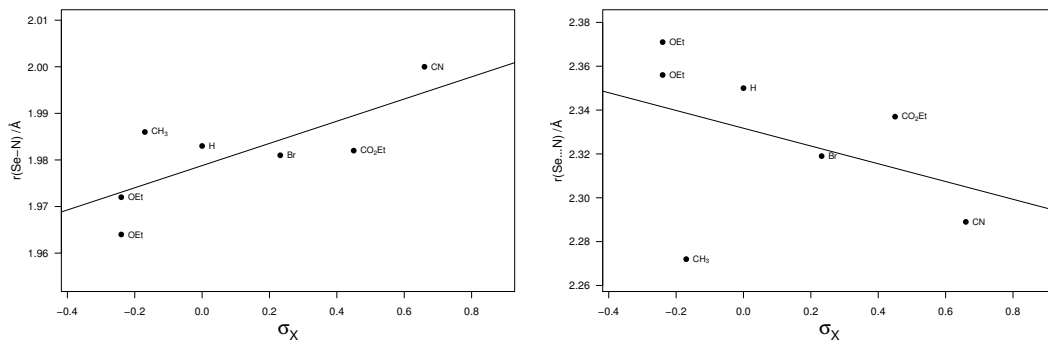


FIGURE 2.4: Hammett plots of endocyclic Se–N bond length and Se···N Ch-bond length of ebselen derivatives complexed with **4a**. The lines are described by the equations $r(\text{Se}-\text{N}) = (1.9788(32) - 0.024(9) \times \sigma_X)$ Å ($R^2 = 0.5722$) and $r(\text{Se}-\text{N}) = (2.331(14) - 0.04(4) \times \sigma_X)$ Å ($R^2 = 0.1588$)

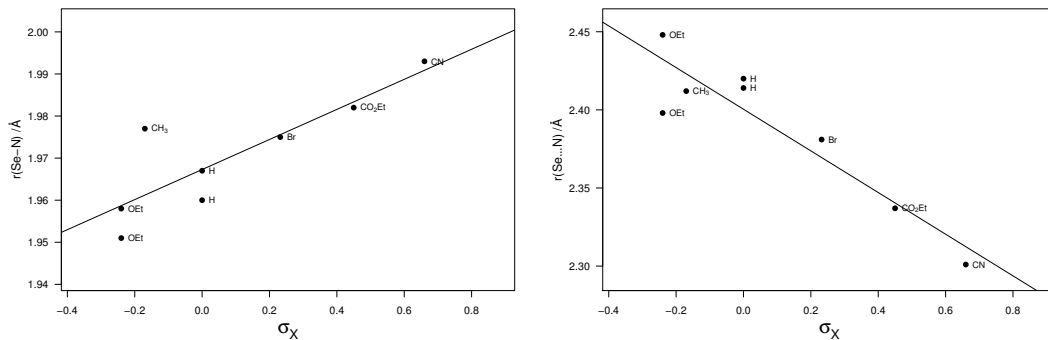


FIGURE 2.5: Hammett plots of endocyclic Se–N bond length and Se···N Ch-bond length of ebselen derivatives complexed with **4b**. The line is described by the equation $r(\text{Se}-\text{N}) = (1.9673(34) - 0.035(10) \times \sigma_X)$ Å ($R^2 = 0.7260$) and $r(\text{Se}-\text{N}) = (2.397(77) - 0.13(2) \times \sigma_X)$ Å ($R^2 = 0.8708$).

Linear regression analysis affords the relationship $r(\text{Se}-\text{N}) = (1.957(5) + 0.054(12) \times \sigma_X)$ Å with a correlation coefficient of 0.6297 for co-crystals with DMAP.

An inverse correlation can be seen in the Se···N Ch-bond length in Figure 2.3. The gradient of the line is now negative and somewhat steeper, at $-0.15(4)$ Å. However the correlation coefficient is decreased to 0.5056. The reason for this is apparent in the left hand side of the plot. While the more strongly Ch-bonded systems (with electron withdrawing substituents) are generally very well described by the regression model, the electron rich derivatives **1j** and **1k** vary significantly in their bond lengths.* Indeed, omitting these data points improves the correlation coefficient to 0.8148 while the gradient and intercept are almost unchanged at

*This is also visible, though less apparent, in the plot of endocyclic bond lengths (Figure 2.3).

$-0.156(28)$ Å and $2.386(15)$ Å respectively, suggesting that the model is appropriate, and that there is some other effect occurring in electron rich systems.

DFT calculations show that the vibrational mode associated with Ch-bond stretching is found at very low energy. The force constant is $5\text{--}10 \mu\text{dyne}\cdot\text{\AA}^{-1}$, which means that the energetic penalty associated with a 0.18 Å deformation (the difference between the shortest and longest Ch-bond length) is only $0.02\text{--}0.03 \text{kcal}\cdot\text{mol}^{-1}$. Crystal packing forces (the sum of weak interactions such as C-H/ π , π/π and C-H/O interactions) are commonly accepted to be in the range of $1\text{--}2 \text{kcal}\cdot\text{mol}^{-1}$, so it is perhaps not surprising that the Ch-bond is deformed by the crystal environment.⁵

That said, there are no obvious differences between the two Ch-bond environments in any of the crystals that display this effect. We performed a solid state IR experiment to probe the crystalline environment surrounding the carbonyl, which is dependent on the Ch-bond environment due to conjugation through the amidic nitrogen ([Figure 2.6](#)).

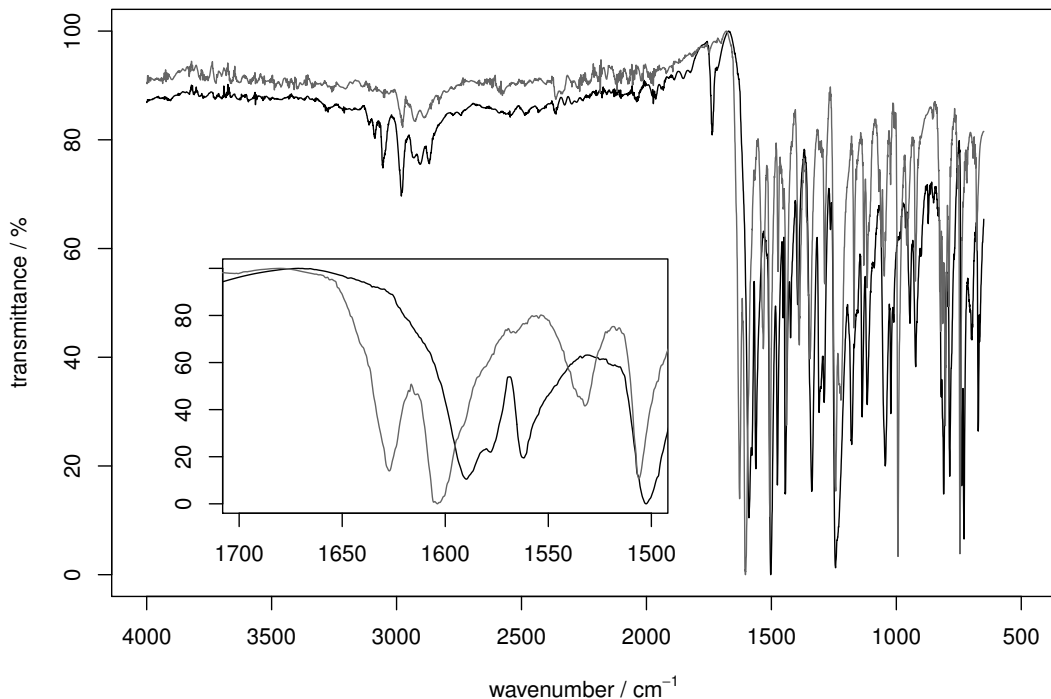


FIGURE 2.6: Solid state IR spectrum of **1k**·DMAP. The spectrum of the pure **1k** is shown in gray.

In the pure compound the carbonyl peak is found at approximately 1590 cm^{-1} and is relatively sharp and well defined. In the co-crystal, we observe the carbonyl peak at higher wavenumber

(1610 cm^{-1}), due to the increased double bond character, as the π system and oxygen lone pair are no longer involved in the Ch-bond. This effect ostensibly outweighs the *decreased* double bond character caused by the shortened Ch-bond formed between the pyridyl nitrogen and selenium (Figure 2.7).

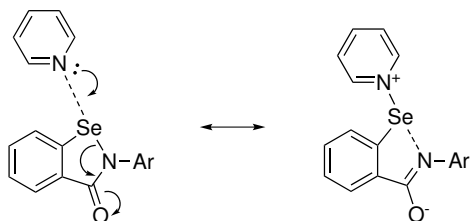


FIGURE 2.7: Contributing resonance form of a Ch-bonded complex with strong Lewis bases.
The double bond character of the carbonyl is decreased.

If there are truly two Ch-bonded environments, we would expect to see splitting or at least broadening of the carbonyl signal in the IR spectrum of the co-crystal. This is not the case, meaning that either the difference is too small to be seen in the spectrum, or the two environments are actually the same, and the measured differences are a crystallographic artefact, either a manifestation of missed symmetry, disorder, or a doubled cell.

However, we do not believe this is likely, for two reasons. Firstly, the data was of extremely high quality, and no alerts were raised in the ADDSYM routine of PLATON. Secondly, a refinement was conducted with a tight SADI restraint on the Ch-bonds ($\sigma = 0.0001$), which forced them to adopt the same length of approximately 1.949 \AA . This increased the R-factor by 1.2%, and significant residual density was visible where the pyridyl nitrogen had been displaced. Furthermore, removal of the restraint recovered the original model, ruling out the possibility of a false minimum.

Solid state NMR of the co-crystal was also used to investigate the crystalline environment. A sample of **1j**·DMAP was first characterised by single crystal x-ray diffraction, which confirmed the polymorph and structural parameters (Figure 2.8).

The bulk material was then crushed and homogenised, and characterised by powder x-ray diffraction. The measured powder pattern was in excellent agreement with the pattern calculated from the single crystal data (Figure 2.9), indicating good phase purity.

Spectra were then acquired using a 400 MHz instrument and triple resonance MAS room temperature probe tuned to ^1H , ^{13}C and ^{77}Se . ^1H - ^{13}C or ^1H - ^{77}Se cross polarisation was used for signal enhancement, and a spin frequency of 10 kHz was used in most cases.

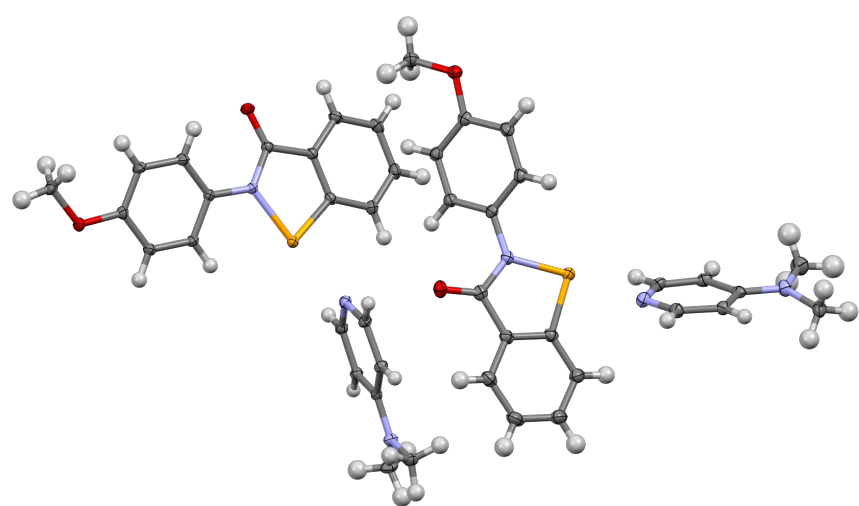


FIGURE 2.8: Single crystal x-ray structure of **1j**·DMAP, displaying the two systems in the asymmetric unit.

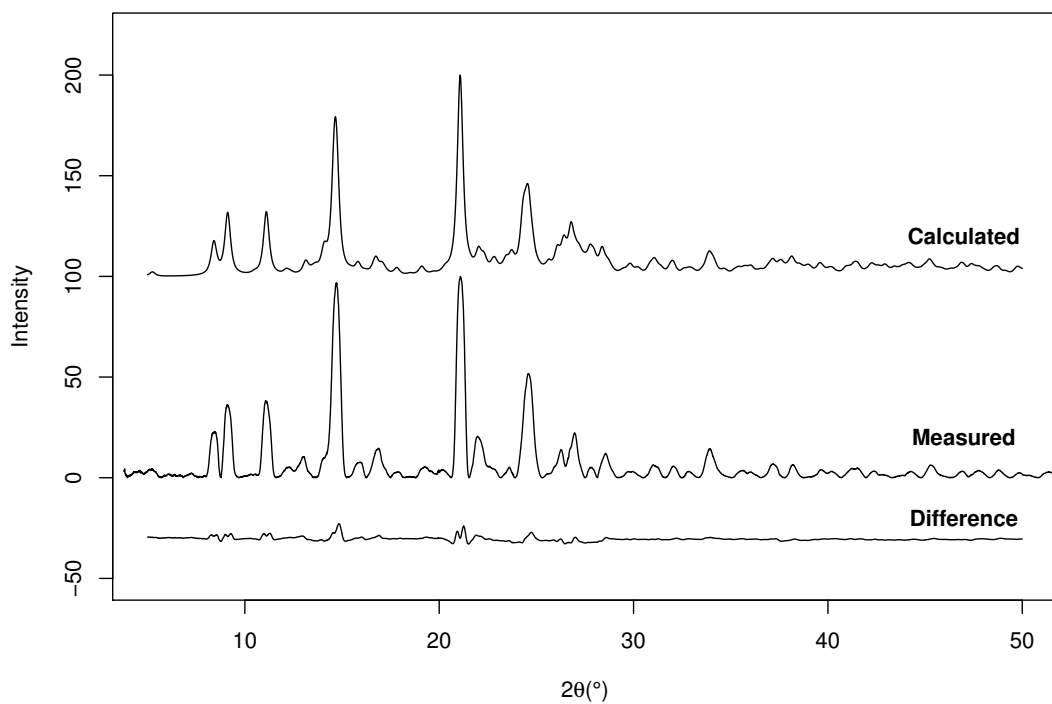


FIGURE 2.9: Calculated vs measured powder diffraction pattern for **1j**·DMAP.

CDCl_3 solution spectra of the complex were also obtained on a 500 MHz instrument. The ^1H and $^1\text{H}-^{13}\text{C}$ HSQC spectra (Figure 2.10) were used to unambiguously assign the ^{13}C spectrum.

The aromatic region of the solid state ^{13}C spectrum is shown in Figure 2.11, overlaid with the corresponding solution spectrum[†]. Good agreement is observed for all signals, with some interesting phenomena visible in the solid state spectrum. Firstly, the signal at 138.62 ppm corresponding to C8 is split into a 1:1:1 triplet, possibly due to coupling to the spin 1 ^{14}N nucleus adjacent. However this is not observed for the C7 signal, nor any signals in the pyridyl ring. Secondly, shoulders can be seen on the C15/C19 and C16/C18 signals. This indicates that the crystalline environment surrounding each DMAP is different, which provides further evidence that there are indeed two systems in the asymmetric unit. The relatively poor resolution of the solid state ^{13}C NMR spectrum limits further analysis, particularly of the C1 signal which is obscured by several other signals.

To conclusively demonstrate that there are two systems in the asymmetric unit we conducted a solid state ^{77}Se NMR experiment, which is shown in Figure 2.12.[‡] In solution, the ^{77}Se resonance is found around 900 ppm relative to dimethylselenide ($\delta = 0$ ppm), and appears as one singlet due to the averaging of all environments. In the solid phase, the spectrum is significantly more complex, primarily due to chemical shift anisotropy which manifests as spinning sidebands. The true anisotropic chemical shifts can only be discerned by varying the MAS spinning speed, which changes the spacing of the sidebands while leaving the parent signals in the same place. Spinning at 12 kHz instead of 10 kHz showed that the signals at 834.69 and 867.02 ppm are the true isotropic chemical shifts, and the fact that there are two signals show that there are indeed two Ch-bonded systems in the asymmetric unit.

2.2.2 Measurement of chemical shift anisotropy

The intensities of the spinning sideband manifold can be analysed to afford the principal values of the chemical shift tensor, that is to say, the shape of the ellipsoid that is described by the tensor. An example is presented in Figure 2.13 of proton decoupled solid state ^{31}P spectra of barium diethyl phosphate, reproduced from the work of Herzfeld and Berger.⁶ In the first spectrum, no magic angle spinning was used, and the lineshape is characteristically broadened due to chemical shift anisotropy. Note the poor S/N ratio due to the broad peak.

[†]The ^{13}C spectrum was referenced to adamantane.

[‡]The ^{77}Se spectrum was referenced to diphenyl diselenide.

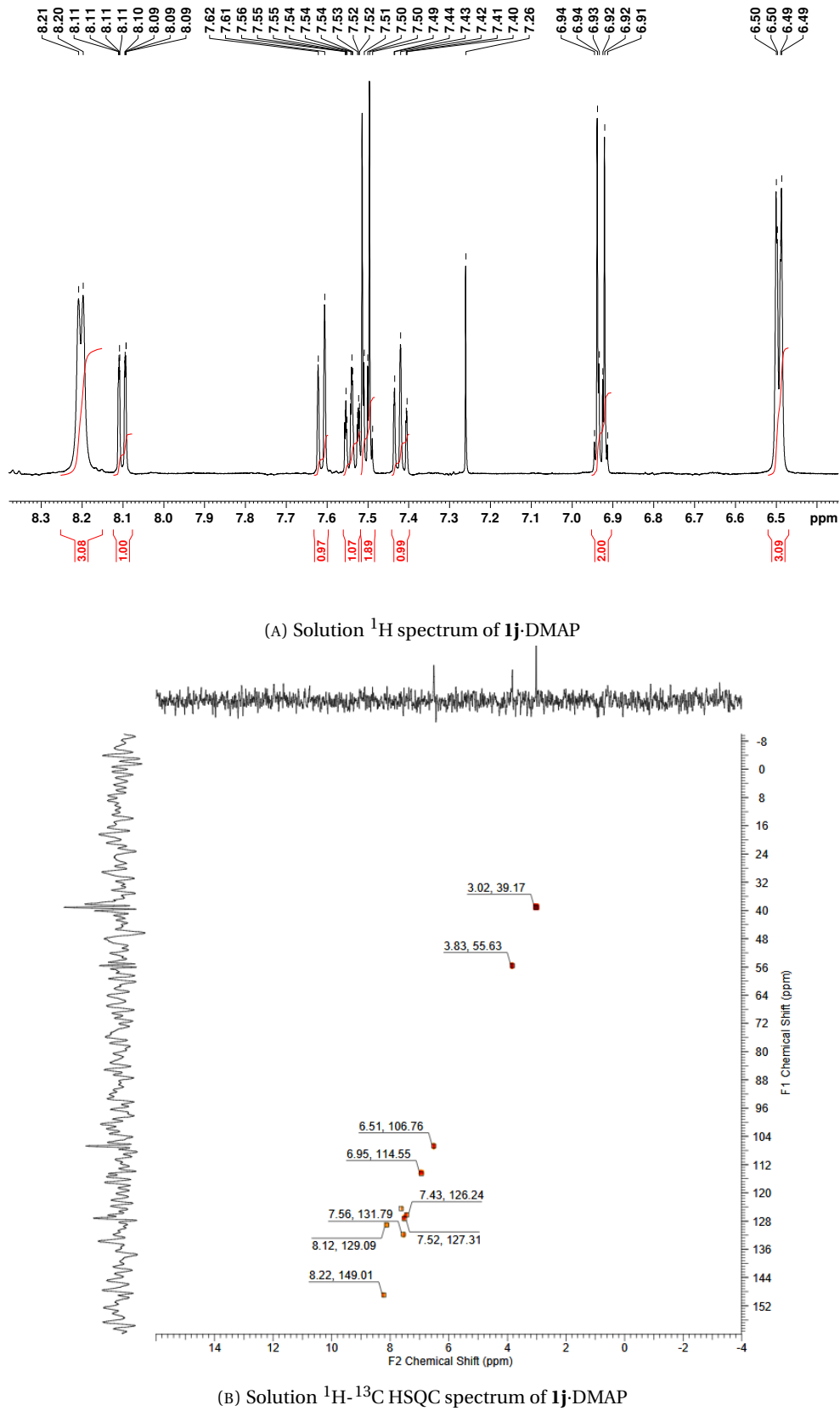


FIGURE 2.10

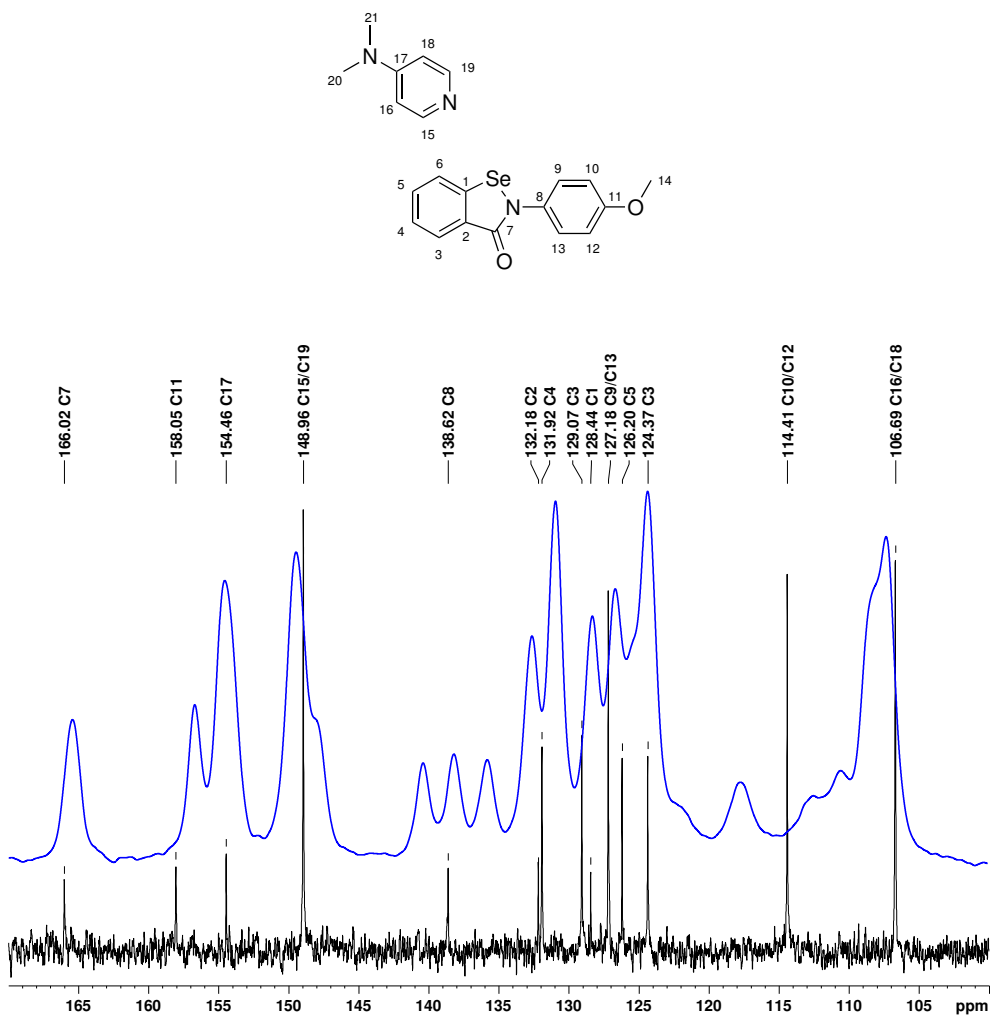


FIGURE 2.11: Solid state ^{13}C -NMR spectrum of **1j**-DMAP (blue) overlaid on solution spectrum of the same (black). Signals are assigned according to the numbering scheme above.

Assuming constant power is deposited in the sample, sharper lines will give improved S/N ratio as the radiated energy is concentrated in narrower bands. The S/N ratio can be seen to improve as the spinning speed increases, and the sidebands become more sparse, affording a stronger signal overall.

The relationship between this lineshape and the chemical shift tensor is shown in Figure 2.14, reproduced from the work of Facelli, Grant, and Michl.⁷ The principal values of the tensor δ_{11} , δ_{22} and δ_{33} correspond to the two extrema of the line, and the central peak. Note that this peak is not the same as the isotropic chemical shift observed in solution, which is given by the average

$$\delta_{iso} = \frac{(\delta_{11} + \delta_{22} + \delta_{33})}{3} \quad (2.1)$$

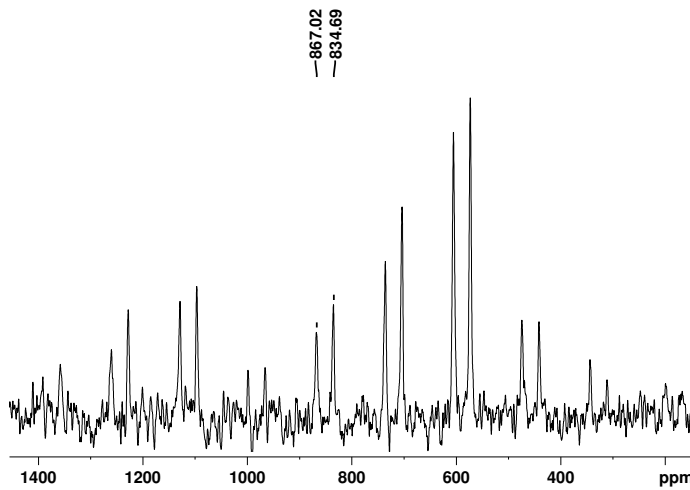


FIGURE 2.12: Solid state ^{77}Se -NMR spectrum of **1j**·DMAP. The primary resonances are visible at 834.69 and 867.02 ppm. The remaining peaks are spinning sidebands, and are separated from the parent signals by multiples of 10 kHz (the magic angle spinning frequency).

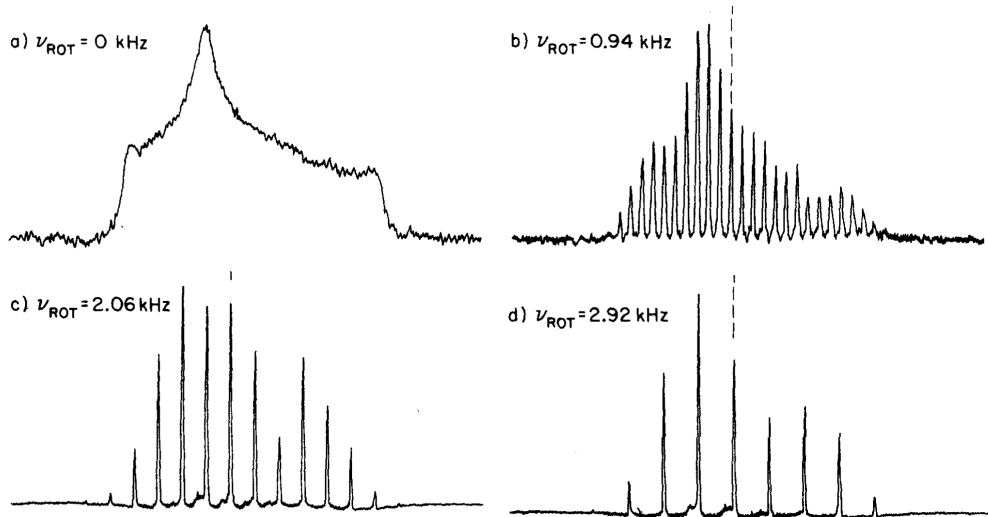


FIGURE 2.13: Proton decoupled solid state ^{31}P spectra of barium diethyl phosphate spinning at the magic angle, at the speed specified. The isotropic chemical shift is shown by the vertical dotted line.

The principal values of the tensor are clearly easily obtained from a non-spinning sample, as they can practically be read off the spectrum. However, the extremely poor S/N ratio (especially for a relatively insensitive nucleus like ^{77}Se) limits the utility of this method. Spinning at the magic angle is clearly necessary to improve the S/N ratio, however this obscures the true locations of the extrema of the lineshape, therefore the values of δ_{11} and δ_{33} , as well as modifying the position of the maximum (δ_{22}).

There exist programs (such as SOLA, integrated within TopSpin by Bruker BioSpin) which can

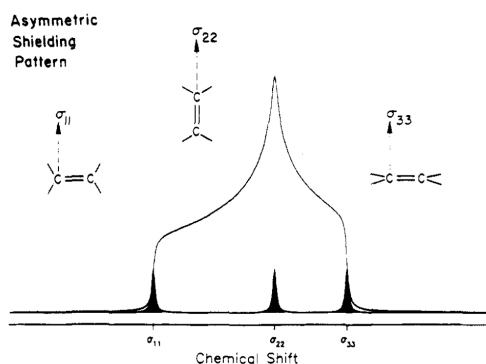


FIGURE 2.14: Characteristic solid-state NMR powder lineshape for an asymmetric tensor e.g. in an alkene. The positions of the three principal values are shown.

fit an experimental lineshape or sideband manifold affording the principal values of the tensor, however there is clearly a trade-off between obtaining a good S/N ratio and having enough sidebands within the limits of the signal for a meaningful fit. Another issue is encountered with preferred orientation of crystallites, as in powder diffraction, which is not modelled in the fitting routine, leading to a poorer fit. Perhaps the most fundamental issue stems from the fact that the sample is a powder of randomly oriented particles. This means that the absolute orientation of the tensor with respect to the molecule cannot be determined from this kind of experiment. Nonetheless, the *shape* of the tensor is still valuable information that may be able to shed light on Ch-bonding in the solid phase.

To this end, we acquired solid state spectra of three complexes spanning the range of electron demand, **1j**·DMAP, **1a**·DMAP, and **1d**·DMAP. § The resulting spectra are presented in Figure 2.15, and the extracted principal values of the chemical shift tensor are presented in Table 2.2.

TABLE 2.2: Principal values of the chemical shift tensor extracted from powder spectra in Figure 2.15.

Complex	δ_{iso}	δ_{11}	δ_{22}	δ_{33}
1j ·DMAP [¶]	835.2	1572.58	466.52	466.50
1j ·DMAP	866.9	1628.91	485.95	485.92
1a ·DMAP	864.5	1616.74	596.21	380.64
1d ·DMAP	860.8	1596.92	547.82	437.66

§ **1j**·DMAP differs from the other structures, in that it crystallises in the space group $P2_1/c$, whereas **1a**·DMAP and **1d**·DMAP both crystallise in $P\bar{1}$. The 2_1 screw axis in the former crystal is oriented such that it generates a symmetry equivalent molecule which is rotated by an angle of about 45° . This means that the observed chemical shift tensor is the average of these two symmetry related orientations, further complicating the analysis. Fundamentally this is due to the fact that an ellipsoid does not have twofold rotational symmetry, except about its principal axes. The triclinic complexes **1a**·DMAP and **1d**·DMAP do not suffer from this issue, as the inversion symmetry operation preserves the shape of the tensor. This can be seen in the latter two principal values of the chemical shift tensor in Table 2.2, which have the same value (within experimental error), describing a cigar-shaped tensor.

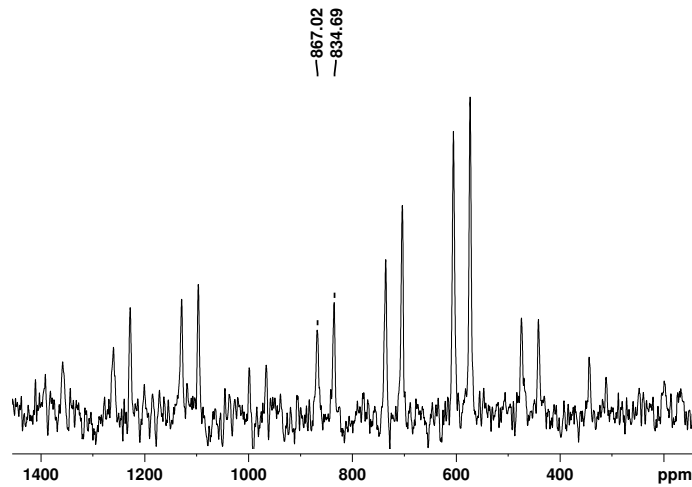
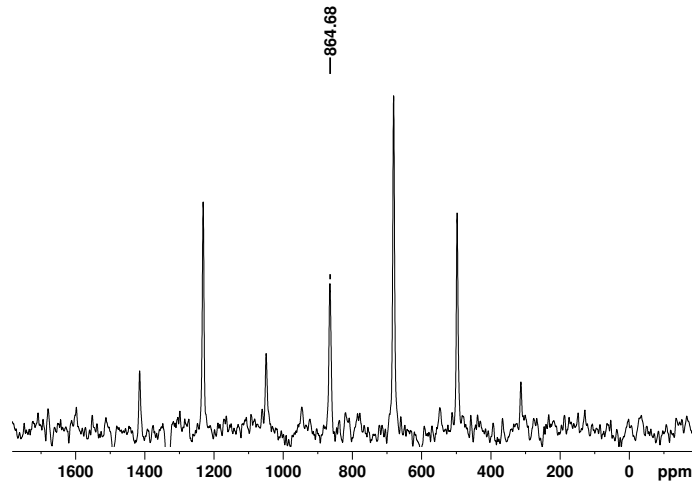
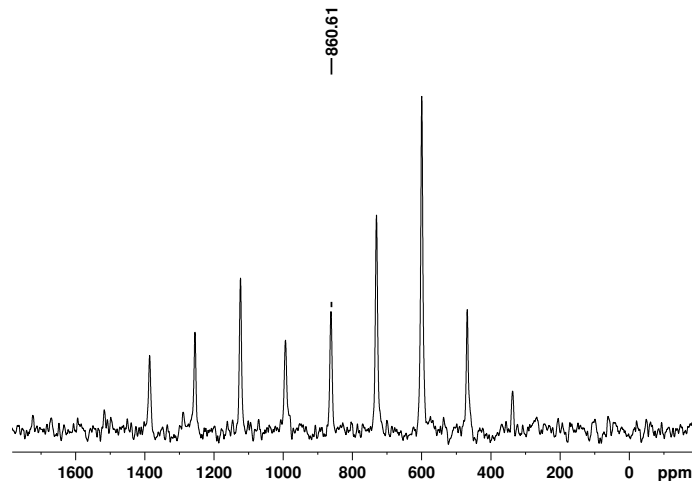
(A) ⁷⁷Se CPMAS NMR spectrum of **1j**·DMAP.(B) ⁷⁷Se CPMAS NMR spectrum of **1a**·DMAP.(C) ⁷⁷Se CPMAS NMR spectrum of **1d**·DMAP.

FIGURE 2.15

In order to verify our results, we also *calculated* the chemical shielding tensors in order to compare the principal values, and also determine the likely orientation of the tensors with respect to the rest of the molecule (Figure 2.16). These calculations were conducted at the ω B97X-D/def2tzvp level, using the GIAO method of calculating shielding tensors.^{8,9} The tensors (in the default reference frame) were found to be

$$\sigma_{\mathbf{1j}\cdot\text{DMAP}} = \begin{bmatrix} 1595.7999 & 367.4957 & 6.7322 \\ 322.6389 & 291.3611 & 10.8588 \\ -19.9165 & -35.8017 & 1069.2648 \end{bmatrix}$$

$$\sigma_{\mathbf{1a}\cdot\text{DMAP}} = \begin{bmatrix} 1595.7999 & 367.4957 & 6.7322 \\ 322.6389 & 291.3611 & 10.8588 \\ -19.9165 & -35.8017 & 1069.2648 \end{bmatrix}$$

$$\sigma_{\mathbf{1d}\cdot\text{DMAP}} = \begin{bmatrix} 1595.7999 & 367.4957 & 6.7322 \\ 322.6389 & 291.3611 & 10.8588 \\ -19.9165 & -35.8017 & 1069.2648 \end{bmatrix}$$

affording reference frame independent principal values in Table 2.3.

TABLE 2.3: Principal values of the chemical shielding tensor calculated from optimised structures.

Complex	σ_{iso}	σ_{11}	σ_{22}	σ_{33}
1j·DMAP	-	-	-	-
1a·DMAP	985.4753	205.5761	1069.2485	1681.6013
1d·DMAP	-	-	-	-

In order to convert these chemical shielding tensors σ into chemical *shifts* δ , we must reference them to a standard σ_{ref} .

$$\delta = 10^6(\sigma_{\text{ref}} - \sigma_{\text{sample}}) \quad (2.2)$$

Convention dictates that for ^{77}Se , dimethylselenide is assigned a chemical shift of 0 ppm. The structure of dimethylselenide was therefore optimised and shielding tensors calculated at the same level.

^aSite a

^bSite b

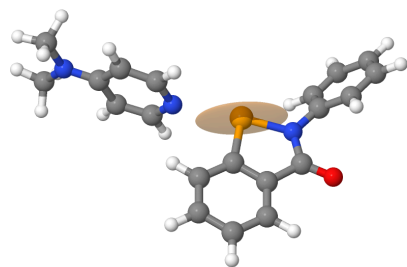


FIGURE 2.16: Calculated chemical shielding tensor for **1a**·DMAP.

2.2.2.1 Measurement of CSA in a single crystal

We were fortunate to obtain a single crystal of **1a**·DMAP of sufficient size (approx $10 \times 3 \times 1$ mm, Figure 2.17) for a single crystal SS-NMR experiment, allowing us to measure the orientation of the tensor in that crystal for comparison with our computational results.^{**} In order to do this, the faces of the crystal had to be indexed to the internal structure. As the crystal was far too big to mount on the diffractometer, two faces were marked with different coloured pens, then a small fragment was removed from the crystal. This was mounted, and a short data collection afforded an indexable pattern. The resulting planes are shown in Figure 2.18, with the internal structure adjacent.



FIGURE 2.17: Single crystal of **1a**·DMAP used for SS-NMR.

2.2.3 Solution-phase studies

While the above crystallographic analysis gives a useful qualitative understanding of the strength of the Ch-bond, we sought an experimental method that could accurately determine bond energies, so that we could easily compare our Ch-bonded complexes with those

^{**}Unfortunately no other derivatives formed crystals of sufficient size or morphology for the SS-NMR experiment.

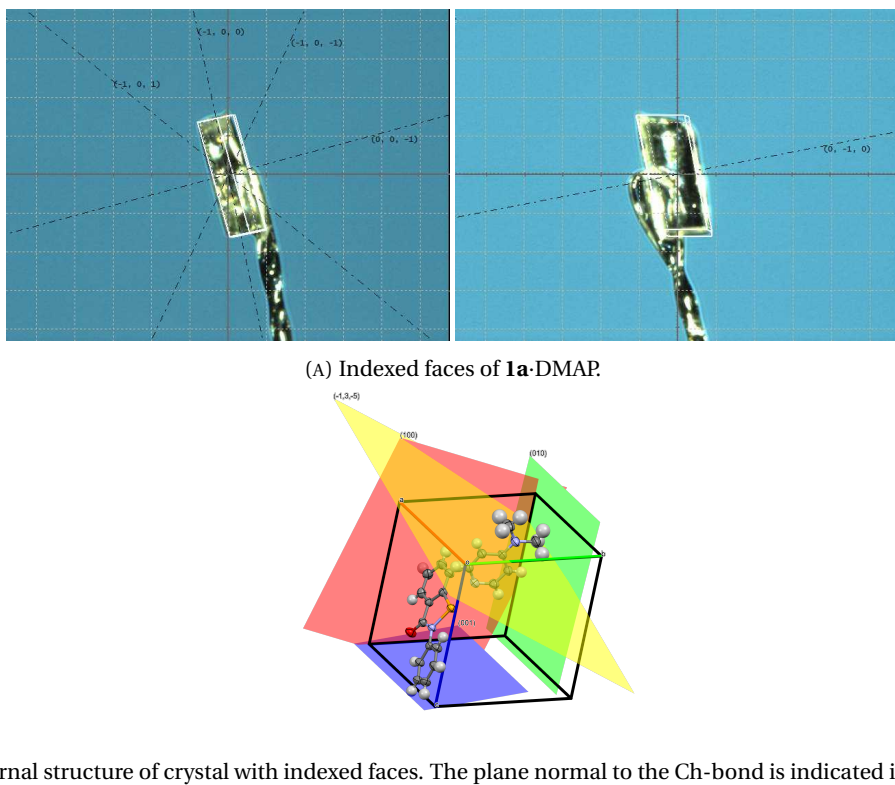


FIGURE 2.18

dominated by other interactions.

2.2.3.1 NMR titration experiments

NMR titrations are a useful tool for the determination of binding affinities in supramolecular and host-guest chemistry. ^1H and ^{19}F NMR have both been used to study halogen bonded systems, however we decided to take advantage of the unique NMR characteristics of the ^{77}Se nucleus to probe the Ch-bond in our systems for the following reasons:

- the nucleus has an extremely wide chemical shift range (-1000–2000 ppm),
- the chemical shift is very sensitive to the electronic environment around the selenium,
- the selenium is at the heart of the interaction, so any electronic changes should manifest clearly,
- the spectrum (for our compounds) is extremely simple, featuring only one singlet,
- the experiment is moderately sensitive (slightly more sensitive than ^{13}C).

We devised a titration experiment, where a solution of a Lewis base is gradually added to a solution of the Ch-bond donor, and the chemical shift of the selenium is measured at the various concentrations of base. As the concentration of base increases, a greater proportion of the selenium species will be in a Ch-bonded environment, with an associated increase in electron density at the selenium due to the coordinated base. This will lead to an upfield shift of the selenium resonance.

It is important to note that even in the absence of a Lewis base, the organoselenium species will still likely feature a Ch-bond to the carbonyl oxygen of another molecule. This interaction can be seen to dominate the crystal packing of ebselen derivatives in the absence of any other coordinating species. This is substantially weaker than a Se...N interaction, but non-negligible. We must therefore view these as *competition* experiments, rather than an absolute measure of binding energy.

For single site binding (a valid approximation for these systems, as the single σ -hole is likely to out-compete all other interactions), the dissociation constant can be expressed as

$$K_d = \frac{[\text{ebs}][\text{base}]}{[\text{ebs} \cdot \text{base}]} \quad (2.3)$$

If the Ch-bond formation/breaking is slow on the NMR timescale, two distinct resonances will be observed that correspond to the “free” (Ch-bonded to a carbonyl oxygen) and “bound” (Ch-bonded to the Lewis base) selenium species, and their relative concentrations can be determined by integration of the signals. As it happens, this is not the case, and the process is fast relative to the NMR timescale. The observed chemical shift is therefore the mole fraction ($f_{\text{ebs}} = [\text{ebs}] / [\text{ebs}]_0$ and $f_{\text{ebs}\cdot\text{base}} = [\text{ebs} \cdot \text{base}] / [\text{ebs}]_0$) weighted average of the chemical shifts of the two species:

$$\delta_{\text{observed}} = \delta_{\text{ebs}} f_{\text{ebs}} + \delta_{\text{ebs}\cdot\text{base}} f_{\text{ebs}\cdot\text{base}} \quad (2.4)$$

If we consider only the *change* in chemical shift from the free species, this becomes simply:

$$\Delta(\delta_{\text{observed}}) = \Delta(\delta_{\text{ebs}\cdot\text{base}}) f_{\text{ebs}\cdot\text{base}} \quad (2.5)$$

$$= \Delta(\delta_{\text{ebs}\cdot\text{base}}) \left(\frac{[\text{ebs} \cdot \text{base}]}{[\text{ebs}]_0} \right) \quad (2.6)$$

From here we can rearrange the equilibrium expression (2.3) and mass balance equation ($[ebs]_0 = [ebs] + [ebs \cdot base]$), and substitute them in to arrive at the generic binding isotherm equation:

$$\Delta(\delta) = \frac{\Delta(\delta_{ebs \cdot base}) \times [base]}{K_d + [base]} \quad (2.7)$$

This assumes that there is insignificant depletion of the base concentration due to complexation.¹⁰ Such an assumption may not be entirely valid for this situation, which may explain the imperfect fitting. However, the analysis is considerably simplified, and adequate standard deviations are obtained using this method.

The resulting K_d values can be converted to free energies:

$$\Delta G = -RT \ln K_d \quad (2.8)$$

A saturated solution of the organoselenium derivative in chloroform was used, due to the high solubility (to reduce acquisition time) and non-coordinating nature (to minimise Ch-bonding to the solvent). This was spiked with a small amount of deuteriochloroform for the lock signal. Spectra were acquired on a 500 MHz instrument, using a 60° pulse and 1 s relaxation delay, until an unambiguous ^{77}Se resonance was observed. The resulting chemical shifts were then tabulated and plotted against the concentration of the Lewis base. These are shown in [Figure 2.19](#).

Non-linear regression analysis was performed with the `nls` function in the R software package using the relationship derived above, and the calculated values are given in [Table 2.4](#).¹¹

TABLE 2.4: Binding energies for complexes of **1b**, **1k**, **1g**, **1a** and **1e** with DMAP, derived from ^{77}Se -NMR titration experiments.

Complex	Binding energy (kcal/mol)	$\Delta(\delta_{ebs \cdot base})$ (ppm)
1b ·DMAP	0.17(6)	41.6
1k ·DMAP	0.47(3)	102.8
1g ·DMAP	0.87(5)	104.2
1a ·DMAP	1.12(4)	70.05
1e ·DMAP	2.28(5)	82.62

Although there is insufficient data to derive clear trends from a Hammett relationship, we can nevertheless visualise the data in a plot, which shows that the Ch-bond gets appreciably stronger with more electron withdrawing substituents ([Figure 2.20](#)).

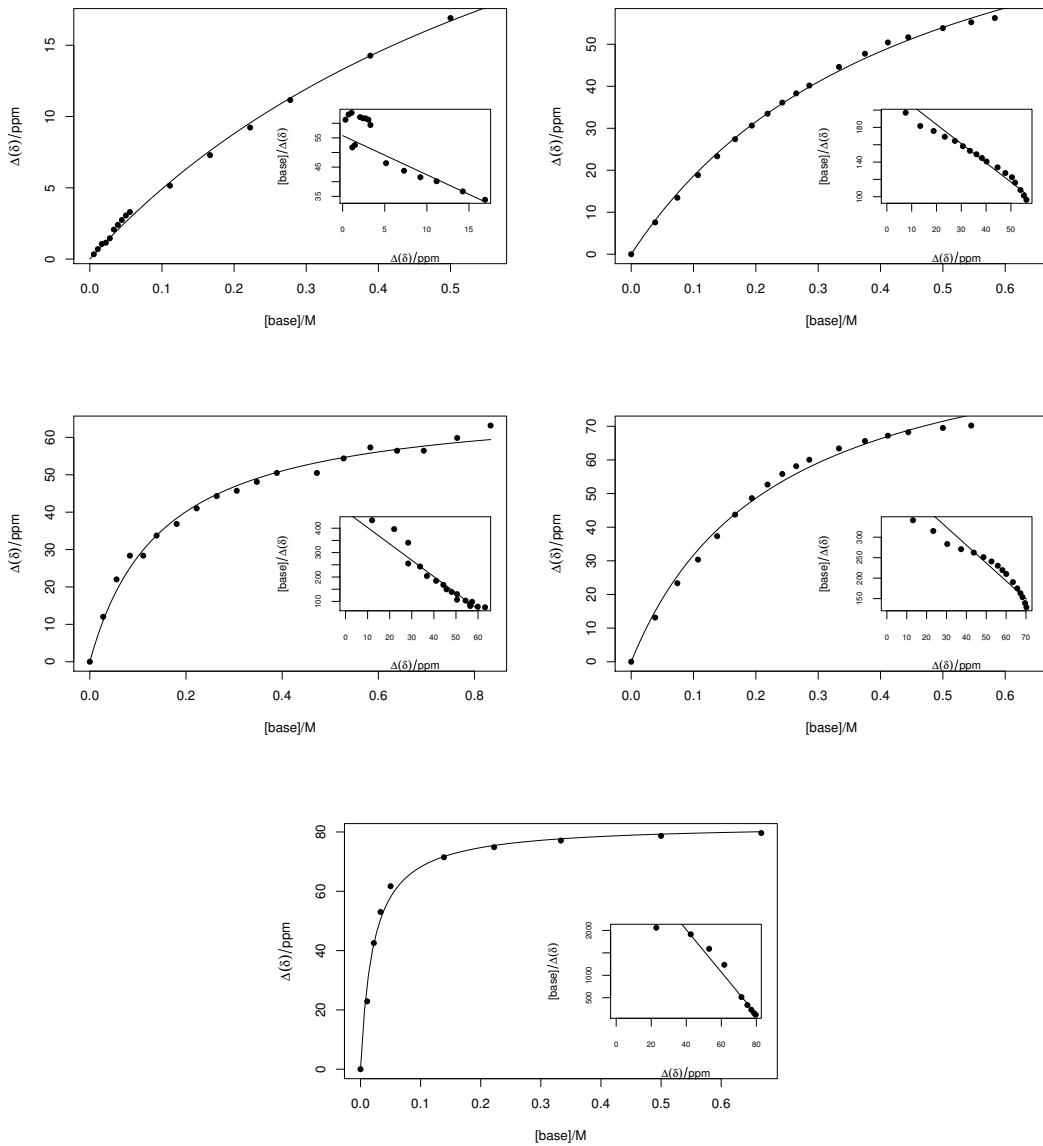


FIGURE 2.19: Binding isotherms for ebselen derivatives **1b**, **1k**, **1a**, **1g** and **1e** with DMAP. Scatchard plots are inset.

2.2.3.2 UV-Vis titration experiment

Although extremely useful, the NMR titration technique had a number of drawbacks. Firstly, relatively large amounts (~ 100 mg) of the Ch-bond donor were required. For simple systems such as these, this was not an issue, however we hoped to apply the technique to less synthetically accessible molecules, which may not be available in such quantities. Secondly, the experiment is quite time consuming, with tens of minutes required per spectrum.

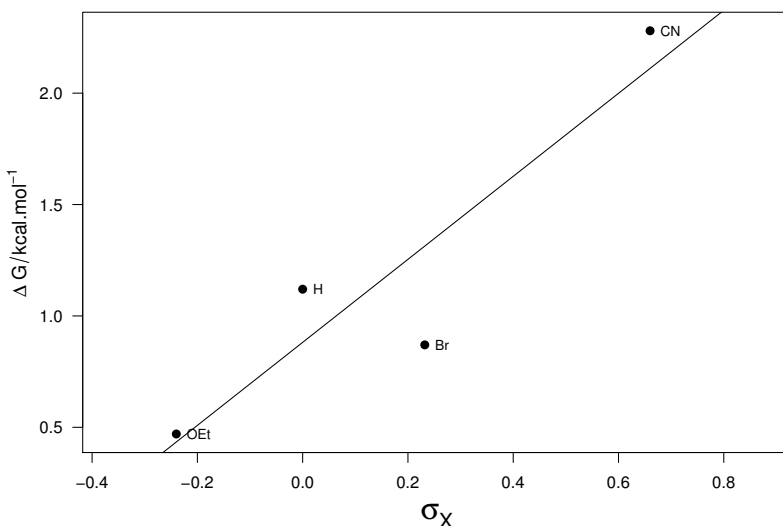


FIGURE 2.20: Hammett plot of binding energies between ebselen derivatives and DMAP, determined by ^{77}Se -NMR titration. The line is described by the equation $\Delta G = (0.88(21) + 1.86(57) \times \sigma_X) \text{ kcal}\cdot\text{mol}^{-1}$ ($R^2 = 0.8437$).

UV-Vis spectroscopy presented a possible solution to both of these issues, with spectra collected in seconds even with extremely dilute solutions. Interactions which have a charge-transfer component (such as Ch-bonding) can give rise to strong absorbances attributable to the $n \rightarrow \sigma^*$ transition.¹² However, we were unable to observe any evidence of such absorbances in our systems. This may be due to the fact that these Ch-bonds are primarily electrostatic in origin, or because the aromatic systems are already strongly absorbing, thus obscuring the charge-transfer band.

2.2.4 Ch-bonding in the gas phase

To complete our trifecta of experiments, we sought evidence that supports Ch-bonding in the gas phase. Broadly, we intended to isolate an ion corresponding to the complex by mass spectrometer, and subsequently fragment it by CID to regain the original species. Naturally, this requires that one (or both) of the components of the complex have a charge, so that it can be detected by the mass spectrometer. We initially injected an equimolar mixture of DMAP and ebselen **1a** in methanol, and isolated an ion of m/z 398.08 a.m.u. However, this could be assigned to either the desired Ch-bonded complex, protonated at the carbonyl oxygen, or to a H-bonded complex. CID of this ion exclusively gave an ion of m/z 123.09 a.m.u., corresponding to protonated DMAP (Figure 2.21). We interpreted this as evidence that we had

formed the H-bonded complex, as migration of the proton on the timescale of a collision is unlikely, and the proton is most likely to remain with the more basic species in the H-bond. Furthermore, a $\text{N}^+ - \text{H} \cdots \text{O}$ hydrogen bonds are very strong (in excess of 15 kcal/mol),¹³ which is likely to out compete Ch-bonding, with estimated bond enthalpies of < 10 kcal/mol in the gas phase.

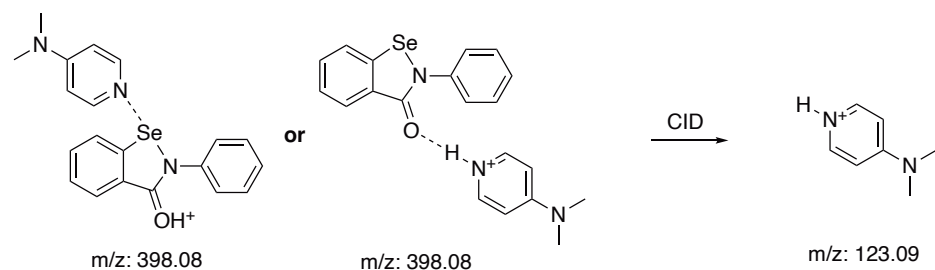


FIGURE 2.21: Dissociation of the complex **1a**·DMAP·H⁺ under CID.

To circumvent this preferential formation of an H-bonded complex, we devised a system with no possibility of H-bonding. The isonicotinate ion was used as the Lewis base, and the complex isolated in the negative ion mode with m/z 397.01 a.m.u. CID of this ion exclusively gave a species of m/z 122.02 a.m.u., corresponding to isonicotinate (Figure 2.22). This provides strong evidence that a Ch-bonded complex is able to be formed in the gas phase.

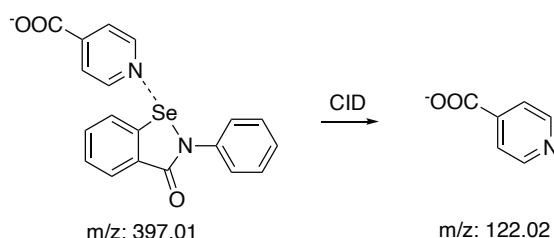


FIGURE 2.22: Dissociation of the complex **1a**·isonicotinate under CID.

Using the technique of CID, one could imagine an experiment where such a Ch-bonded complex is fragmented with gradually increasing energy, and the yield of the product ion measured. This could theoretically be correlated with the gas phase bond energy. Indeed, this is the basis of the technique of Threshold CID (TCID) developed by Armentrout.^{14–16} Although the experiment is simple, the data analysis is not. This is due to the often poorly characterised energy distribution of the reactant ions, and vibrational energy redistribution in the products. These barriers are not insurmountable for simple systems (the technique has been successfully applied to metal complexes, and small non-covalent complexes), but in our moderately complex molecules with many vibrational modes, errors are likely to dominate any values extracted from the experiment. However, we present here a proof of concept

experiment, which shows the decrease in reactant ion intensity and increase in product ion as CID energy is increased ([Figure 2.23](#)).

TODO

FIGURE 2.23: Rudimentary TCID experiment of **1a**-isonicotinate.

2.3 Supplementary materials

2.3.1 Synthetic procedures

2.3.1.1 Preparation of bis(2-carboxyphenyl)diselenide **5**

Anthranilic acid (3.460 g, 25.33 mmol) was dissolved in 1 M hydrochloric acid (80 mL) and cooled to 0°C. Sodium nitrite (1.751 g, 25.37 mmol) in water (40 mL) was then added drop-wise with stirring. The mixture was kept at 0°C.

Selenium (2.080 g, 26.34 mmol) was suspended in 1 M sodium hydroxide (120 mL) and degassed by repeatedly evacuating the flask until the solvent began to boil, then backfilling with N₂. One grain of sodium borohydride was added under N₂ counter flow, followed by hydrazine hydrate (1.3 mL, 26 mmol). The mixture was heated until a red colour appeared, then cooled to 0°C.

The diazonium solution was neutralised with a solution of sodium hydroxide (4.320 g, 108.0 mmol) in water (20 mL), then added slowly to the cooled diselenide solution. Upon completion, the mixture was warmed to room temperature and stirred for 1 h, then neutralised with concentrated hydrochloric acid. The dense precipitate was separated by centrifuging, the supernatant decanted off, and the residue resuspended in hot methanol (300 mL). The methanol solution was subjected to hot filtration, and the orange filtrate concentrated to a volume of ~100 mL. This was cooled to -20°C, and the resulting crystals filtered off and dried. Recrystallisation from methanol gave **5** as a pale brown powder (1.8718 g, 37%).

¹H NMR (400 MHz, *d*₆-DMSO) δ ppm 7.29–7.38 (m, 1 H), 7.47 (t, *J*=7.43 Hz, 1 H), 7.66 (d, *J*=8.22 Hz, 1 H), 8.02 (d, *J*=7.43 Hz, 1 H) 13.70 (br. s., 1 H).

MS (ESI +ve) m/z 424.8806 (MNa⁺) C₁₄H₁₁O₄Se₂⁺ requires 424.8802 (Δ=0.941 ppm).

2.3.1.2 Preparation of 2-(chlorocarbonyl)phenylselenyl chloride **6**

Diselenide **5** (1.4758 g, 3.6881 mmol) was dissolved in thionyl chloride (10 ml) with 2 drops DMF and heated to reflux for 90 minutes. The excess thionyl chloride was distilled off under reduced pressure, and the solid residue extracted into dry hexane (30 mL). Evaporation of the solvent afforded **6** as yellow crystals (1.870 g, 100%), which were used without further purification or characterisation.

2.3.1.3 General procedure for the preparation of benzisoselenazolinone derivatives **1a**, **1e**, **1f**, **1g**, **1h**, **1j** and **1k** (procedure A)

The appropriate amine (2.5 mmol) was dissolved in anhydrous acetonitrile (5 mL) and cooled to 0°C. To this was added triethylamine (1 mL, distilled from CaH₂), followed by **6** (2.5 mmol) in a further 5 mL anhydrous acetonitrile. The mixture was stirred at room temperature for 2 h, then the solvent was removed under vacuum. The solid residue was triturated with water (5 mL) and 1 M hydrochloric acid to afford a friable solid, which was purified by recrystallisation from ethyl acetate at -20° C to afford the pure benzisoselenazolinone derivative.

2.3.1.4 Procedure for the preparation of benzisoselenazolinone derivative **1d** (procedure B).

Sodium hydride (60% suspension in mineral oil, 125.0 mg, 3.125 mmol) was suspended in anhydrous THF (5 mL) and cooled to 0°C. 4-Nitroaniline (treated with charcoal and crystallised from aqueous ethanol, 277 mg, 2.01 mmol) was then added and the resulting dark red suspension stirred for 5 minutes at 0°C. DMAP (16.3 mg, 0.133 mmol) was then added, followed by a solution of the dichloride **6** (2.00 mmol) in a further 5 mL anhydrous THF. The mixture was then warmed to room temperature, and stirred for 18 h to give a light yellow suspension, which was quenched with methanol (5 mL), then suspended in water (50 mL). The resulting solid was filtered off, washed with 1 M HCl and water, then dried to give a light yellow powder (336.0 mg, 52%).

Ebselen 1a Colourless crystals, m.p. 182.1–182.3°C (α polymorph), 173.4–174.6°C (β and γ polymorph), xx%.

¹H NMR (499 MHz, *d*₆-DMSO) δ ppm 8.07 (1H, d, *J* = 8.02 Hz), 7.90 (1H, d, *J* = 7.45 Hz), 7.68 (1H, t, *J* = 7.25 Hz), 7.61 (2H, d, *J* = 7.68 Hz), 7.52–7.42 (3H, m), 7.26 (1H, t, *J* = 7.39 Hz).

4-Nitro ebselen 1d Pale yellow crystals, 52%.

¹H NMR (400 MHz, CDCl₃) δ ppm 8.30 (2H, d, *J* = 9.07 Hz), 8.14 (1H, d, *J* = 7.82 Hz), 7.92 (2H, d, *J* = 9.07 Hz), 7.75–7.66 (2H, m), 7.52 (1H, t, *J* = 6.8 Hz).

¹H NMR (499 MHz, *d*₆-DMSO) δ ppm 8.30 (2H, d, *J* = 9.15 Hz), 8.18 (1H, d, *J* = 8.08 Hz), 8.05 (2H, d, *J* = 9.16 Hz), 7.94 (1H, d, *J* = 7.72 Hz), 7.71 (1H, t, *J* = 7.02 Hz), 7.5 (1H, t, *J* = 7.45 Hz).

MS (ESI +ve) m/z 400.0005 (MNa⁺ + acetone) C₁₆H₁₄N₂NaO₄Se⁺ requires 401.00110 (Δ=1.52 ppm).

4-Cyano ebselen 1e Colourless crystals, m.p. 191°C (dec.), 61%. ¹H NMR (600 MHz, *d*₆-DMSO) δ ppm 8.20 (1H, d, *J* = 8.08 Hz), 7.94–7.83 (5H, m), 7.65 (1H, t, *J* = 7.61 Hz), 7.45 (1H, t, *J* = 7.42 Hz).

¹³C NMR (151 MHz, *d*₆-DMSO) δ ppm 166.03, 145.18, 139.4, 133.88, 133.81, 133.03, 129.37, 128.47, 126.78, 126.74, 124.28, 119.20, 114.08, 107.18.

⁷⁷Se NMR (95 MHz, *d*₆-DMSO) δ ppm 897.93.

1e·DMAP m.p. 157.6–160.2°C (DCM solvate, P2₁/c).

1e·DMAP m.p. 176.0–178.8°C (non-solvate, Pbca).

4-Trifluoromethyl ebselen 1f Colourless crystals, m.p. 184.6–186.4°C, 14%.

¹H NMR (499 MHz, *d*₆-DMSO) δ ppm 8.27 (1H, d, *J* = 7.41 Hz), 8.01–7.96 (1H, m), 7.95–7.89 (1H, m), 7.88–7.81 (3H, m), 7.76 (2H, d, *J* = 8.41 Hz).

1f·DMAP m.p. 178.3–179.6°C.

4-Bromo ebselen 1g Colourless crystals, m.p. 189.7–190.7°C, 18%.

1g·DMAP m.p. 162.3–164.4°C.

4-Carboxyethyl ebselen 1h Colourless crystals, m.p. 173.1–174.5°C 13%.

¹H NMR (500 MHz, DMSO-*d*6) δ 8.08 (d, *J* = 7.8 Hz, 1H), 8.02 (d, *J* = 8.7 Hz, 2H), 7.92 (dd, *J* = 0.4, 8.0 Hz, 1H), 7.88 (d, *J* = 8.6 Hz, 2H), 7.71 (t, *J* = 7.0 Hz, 1H), 7.50 (t, *J* = 7.3 Hz, 1H), 4.32 (q, *J* = 7.2 Hz, 2H), 1.33 (t, *J* = 7.1 Hz, 3H).

1h·DMAP m.p. 136.0–138.7°C.

4-Methyl ebselen 1i Light brown crystals, 58%.

¹H NMR (400 MHz, DMSO-*d*6) δ 8.06 (d, *J* = 8.0 Hz, 1H), 7.87 (d, *J* = 7.3 Hz, 1H), 7.66 (dt, *J* = 0.3, 7.4 Hz, 1H), 7.48 (d, *J* = 8.3 Hz, 2H), 7.46 (t, *J* = 7.3 Hz, 1H), 7.24 (d, *J* = 8.2 Hz, 2H), 2.31 (s, 3H).

4-Methoxy ebselen 1j Light brown crystals, 67%.

¹H NMR (500 MHz, DMSO-*d*6) δ 8.07 (d, *J* = 7.9 Hz, 1H), 7.88 (d, *J* = 7.6 Hz, 1H), 7.67 (t, *J* = 7.1 Hz, 1H), 7.49 (d, *J* = 8.4 Hz, 2H), 7.47 (t, *J* = 6.9 Hz, 1H), 7.01 (d, *J* = 8.6 Hz, 2H), 3.78 (s, 3H).

4-Ethoxy ebselen 1k Light brown crystals, 67%.

¹H NMR (500 MHz, DMSO-*d*6) δ 8.06 (d, *J* = 8.0 Hz, 1H), 7.87 (d, *J* = 7.5 Hz, 1H), 7.67 (t, *J* = 7.2 Hz, 1H), 7.48 (t, *J* = 3.2 Hz, 1H), 7.47 (d, *J* = 8.8 Hz, 2H), 6.99 (d, *J* = 8.8 Hz, 2H), 4.05 (q, *J* = 7.0 Hz, 2H), 1.34 (t, *J* = 6.9 Hz, 3H).

2.3.2 Crystallisation methods

Crystals of sufficient quality for x-ray diffraction analysis were grown by vapour diffusion of pentane into a dichloromethane solution (~50 mg/mL) of either the pure Ch-bond donor, or a 1:1 mixture of the donor and the appropriate Lewis base, with the following exceptions:

- the non-solvate of **1e·DMAP** was grown by slow evaporation from THF,
- second polymorphs of **1k·DMAP** and **1j·DMAP** were grown from diffusion of pentane into diethyl ether.

References

- (1) Wei, Y.; Sastry, G. N.; Zipse, H. *Journal of the American Chemical Society* **2008**, *130*, 3473–3477.
- (2) Berthelot, M.; Laurence, C.; Safar, M.; Besseau, F. *Journal of the Chemical Society, Perkin Transactions 2* **1998**, 283–290.
- (3) Heinrich, M. R.; Klisa, H. S.; Mayr, H.; Steglich, W.; Zipse, H. *Angewandte Chemie International Edition* **2003**, *42*, 4826–4828.
- (4) Pedia, W.
- (5) Dunitz, J. D.; Maverick, E. F.; Trueblood, K. N. *Atomic Motions in Molecular Crystals from Diffraction Measurements*, 1988.
- (6) Herzfeld, J.; Berger, A. E. *The Journal of Chemical Physics* **1980**, *73*, 6021–6030.
- (7) Facelli, J. C.; Grant, D. M.; Michl, J. *Accounts of Chemical Research* **1987**, *20*, 152–158.
- (8) Schreckenbach, G.; Ziegler, T. *The Journal of Physical Chemistry* **1995**, *99*, 606–611.
- (9) Schreckenbach, G.; Ziegler, T. *International Journal of Quantum Chemistry* **1996**, *60*, 753–766.
- (10) Thordarson, P. *Chem. Soc. Rev.* **2011**, *40*, 1305–1323.
- (11) R Core Team R: A Language and Environment for Statistical Computing, Vienna, Austria, 2019.
- (12) Blackstock, S. C.; Lorand, J. P.; Kochi, J. K. *Journal of Organic Chemistry* **1987**, *52*, 1451–1460.
- (13) Emsley, J. *Chemical Society Reviews* **1980**, *9*, 91–124.
- (14) Armentrout, P. B. In *Modern Mass Spectrometry*; Springer: Berlin, Heidelberg, 2003, pp 233–262.
- (15) Rodgers, M. T.; Armentrout, P. B. *Mass Spectrometry Reviews* **2000**, *19*, 215–247.
- (16) Narancic, S.; Bach, A.; Chen, P. *Journal of Physical Chemistry A* **2007**, *111*, 7006–7013.